ELSEVIER

Journal of Fluids and Structures 21 (2005) 363–394

JOURNAL OF FLUIDS AND STRUCTURES

www.elsevier.com/locate/jfs

Determination of flow configurations and fluid forces acting on two staggered circular cylinders of equal diameter in cross-flow

Md. Mahbub Alam[a,*], H. Sakamoto[b], Y. Zhou[a]

[a]*Department of Mechanical Engineering, The Hong Kong Polytechnic University, Hung Hom, Kowloon, Hong Kong*
[b]*Department of Mechanical Engineering, Kitami Institute of Technology, 165 Koen-cho, Kitam-shi, Hokkaido 090-8507, Japan*

Received 23 January 2004; accepted 21 July 2005
Available online 10 October 2005

Abstract

Experiments have been carried out to investigate characteristics of flow and fluid forces acting on two circular cylinders in a wide range of staggered configuration. Time-averaged and fluctuating fluid forces acting on the upstream and downstream cylinders were measured for staggered angles $\alpha = 10^\circ$, 25°, 45°, 60° and 75° in the range of $T/D = 0.1$–5.0, where α is the angle between the free-stream flow and the line connecting the centers of the cylinders, T is the gap width between the cylinders, and D is the diameter of a cylinder. Fluid forces acting on the cylinders in staggered configurations were measured in wind-tunnel tests at a Reynolds number of 5.5×10^4 and, then the dependence of magnitudes and trends of fluid force coefficients on the spacing ratio T/D are discussed in light of flow configurations determined on the basis of time-averaged and fluctuating surface pressure, surface oil-flow patterns, and flow visualization patterns. At very small T/D, lift forces depend largely on the gap flow between the cylinders, irrespective of the α value. It is found that the intermittent formation and burst of the separation bubble on the upstream or downstream cylinder is responsible for the bistability of the flow. The flow structure jump from one stable state to another appears discontinuous and is always associated with a change from the presence to absence of a separation bubble around a cylinder or vice versa. Maximum fluctuating drag force acting on the downstream cylinder occurs at $\alpha = 10^\circ$, $T/D = 2.4$–3.0 where the inner shear layer of the upstream cylinder rolls just a little forward of the front surface of the downstream cylinder.

Keywords: Fluid forces; Staggered configuration; Circular cylinders

1. Introduction

Most structures on land and in the ocean are in multiple forms, and fluid–flow interaction on the multiple structures is very complex; yet it has not been studied much. In many engineering applications of cylinder-like structures, i.e., groups of chimney stacks, tubes in heat exchangers, overhead power-line bundles, bridge piers, stays, masts, chemical reaction towers, offshore platforms, adjacent skyscrapers, etc., fluid forces, Strouhal frequencies and flow configurations are major criteria for the design of the structures. The steady and fluctuating fluid forces acting on structures are mainly governed by the characteristics of the flow around them. The alternate shedding of vortices in the

*Corresponding author. Tel.: +852 2766 7813; fax: +852 2365 4703.
E-mail address: mmalam@poyu.edu.hk (M.M. Alam).

0889-9746/$ - see front matter © 2005 Elsevier Ltd. All rights reserved.
doi:10.1016/j.jfluidstructs.2005.07.009

near-wake leads to larger fluctuating pressure forces on the structures and may cause structural vibrations, acoustic noise, or resonance, which in some cases can trigger failure. The cost associated with a typical practical failure can easily be of the order of a million dollars. Thus, it is not surprising that extensive effort is needed to be focused to examine fluid forces, vortex dynamics and the flow configuration around multiple structures. Because of mutual interference, the flow around a group of structures may exhibit many interesting and unexpected phenomena. A pair of two cylinders in various arrangements can be chosen as the simplest case of a group of structures. A thorough understanding of characteristics of fluid flow and vortex dynamics around such a simple case may be crucial to understand the flow around more complex and larger-scale structures. This paper presents a detailed investigation into the steady and fluctuating fluid forces, steady and fluctuating surface pressures and flow configurations of two staggered circular cylinders.

1.1. Review of previous works

Though a staggered arrangement is perhaps the configuration most commonly found in engineering applications, numerous investigations on the flow past two circular cylinders in side-by-side and tandem arrangements have been performed, but investigations pertaining to two staggered cylinders are relatively few. Zdravkovich (1977) and Chen (1986) reviewed a number of papers pertaining to interaction of flow on two cylinders in various arrangements. Depending on the interference effect between the two cylinders, Zdravkovich (1984) and Medeiros and Zdravkovich (1992) divided the whole region of possible arrangements of two cylinders into four regions; (i) the proximity interference region, where the flow around one cylinder affects the other; proximity interference occurs in both side-by-side and slightly staggered cylinders; (ii) the wake interference region, which occurs in tandem and slightly staggered arrangements at spacings such that the near-wake flow of the upstream cylinder is unaffected by the downstream one; however, the downstream one is significantly affected by the upstream cylinder; (iii) the proximity and wake interference region which, in essence, includes the combination of proximity and wake interference; proximity and wake interference occurs in tandem and staggered arrangements for small spacings for which the near wake of the upstream cylinder is disrupted by the downstream cylinder; (iv) the no interference region, where the wake of one cylinder does not affect the other.

Time-averaged drag and lift forces acting on two staggered cylinders were measured by Hori (1959), Cooper (1973), Wardlaw and Cooper (1973), Price (1976), Zdravkovich and Pridden (1977), Zdravkovich (1980), Bokaian and Geoola (1984), Price and Paidoussis (1984), Abdulhadi (1985), Moriya and Sakamoto (1985), Ko and Wong (1992) and Gu et al. (1993). However, their data were mostly concerned with the downstream cylinder. Most of the researchers mainly focused their attention on discussing the flow configuration for the regions in which the so-called 'inner' and 'outer' lift peaks, maximum lift coefficient region, form in a contour map of steady lift force in T/D-α plane, where the symbols are defined in Fig. 1. The explanation for the lift peaks has been provided in different ways by different researchers.

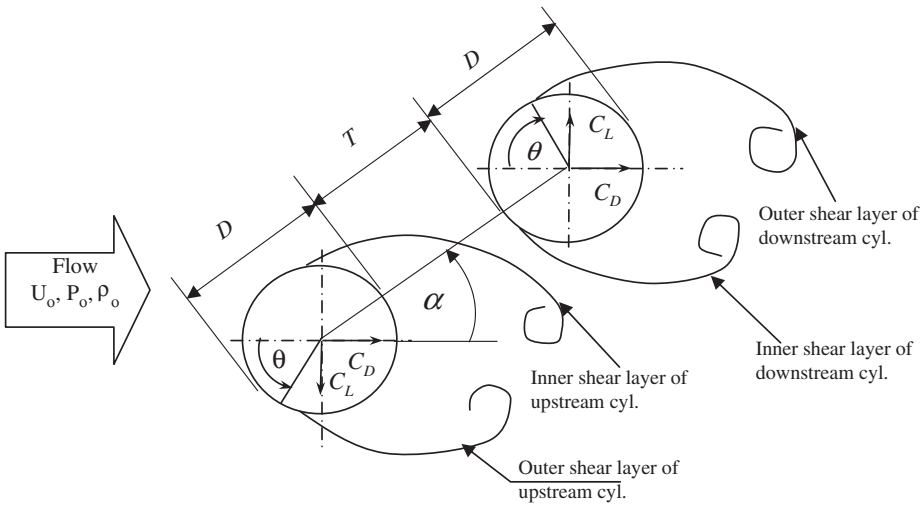

Fig. 1. Notation for staggered configuration.

A summarizing of the different explanations is found in Ting et al. (1998). Though the fluctuating lift and drag forces acting on structures are a major cause of the fatigue failure of the structures and are used for predicting flow-induced responses, the data of fluctuating lift and drag forces acting on two staggered cylinders are very scarce (Chen, 1986). Gu and Sun (1999) recently measured time-averaged pressure on two staggered cylinders and the velocities in the wake at high subcritical Reynolds numbers. They observed two switching flows and three different pressure distributions (patterns I_B, II_B, III_B) on the downstream cylinder from $\alpha = 0^\circ$ (in tandem) to $\alpha = 90^\circ$ (side-by-side). The flow structure that corresponds to the three different pressure distributions is schematically illustrated in Fig. 2 [also see Zdravkovich (1977)]. As seen in the figure, the thickness of a shear layer can be divided into three slices: highly turbulent inner slice, high velocity middle slice and outer slice close to the free-stream. Three different flow structures are identified, depending on which slice of the shear layer sweeps over the inner surface of the downstream cylinder (Gu and Sun, 1999). When only the turbulent slice of the shear layer sweeps over the inner surface of the downstream cylinder, the downstream cylinder is almost completely submerged in the wake of the upstream cylinder and no stagnation point (pressure coefficient = 1.0) occurs, the corresponding flow structure being referred to as pattern I_B. If the high velocity middle slice joins the turbulent inner slice, a stagnation point occurs on the outer surface of the downstream cylinder and a high suction pressure is developed on the inner surface, resulting in pattern II_B. The flow structure is referred to as pattern III_B when the high velocity middle slice and the turbulent inner slice are joined by part of the free-stream slice. Patterns I_B, II_B and III_B occur for $\alpha = 0$–9.65°, 9.7–15°, and 16–90°, respectively, at $T/D = 0.7$ ($\mathrm{Re} = 2.2 \times 10^5$); the critical α, depending on both T/D and Re, is 9.65–9.7° for the transition from pattern I_B to II_B, and 15–16° for the transition from II_B to III_B. Akosile and Sumner (2003), recently, measured time-averaged drag and lift forces acting on two circular cylinders for constant $T/D = 0.125$ and 0.25 with varying α from $\alpha = 0$ to 90°, in both uniform and shear flow, and they recognized several critical angles where the fluid forces jump discontinuously.

With regard to the vortex-shedding frequencies and wake structure behind the two staggered cylinders, the feature of the flow over and behind the cylinders is very complex. The vortex-shedding frequencies and flow structure behind two cylinders have been reported by Ishigai et al. (1972), Kiya et al. (1980), Bokaian and Geoola (1984), Ko and Wong (1992), Sun et al. (1992), Gu and Sun (1999), Sumner et al. (2000) and Sumner and Richard (2003). Alam and Sakamoto (2005) have recently conducted a systematic investigation of Strouhal numbers behind two staggered circular cylinders and behind a circular and a square cylinder in tandem and staggered configurations.

1.2. Scope of this study

The above review indicates that (i) there is a lack for steady drag and lift data for the upstream cylinder, (ii) the information on fluctuating lift and drag forces on either cylinder is very limited, (iii) many aspects of the flow structure around two staggered cylinders have yet to be explored. To address these issues, this work aims (i) to measure steady and fluctuating fluid forces acting on two cylinders in staggered arrangement, (ii) to elucidate the flow structure on and behind the cylinders, and (iii) to present a discussion on the relation between fluid forces and the flow structure. Measurements were conducted at $\alpha = 10^\circ$, 25°, 45°, 60° and 75° and $T/D = 0.1$–5.0. The present study presents a series of measurement results of steady and fluctuating fluid forces, surface pressure distributions, surface oil-flow patterns and flow visualization. The fluid force measurement is further connected with that of the flow structure, and the interactions between the two staggered cylinders are examined.

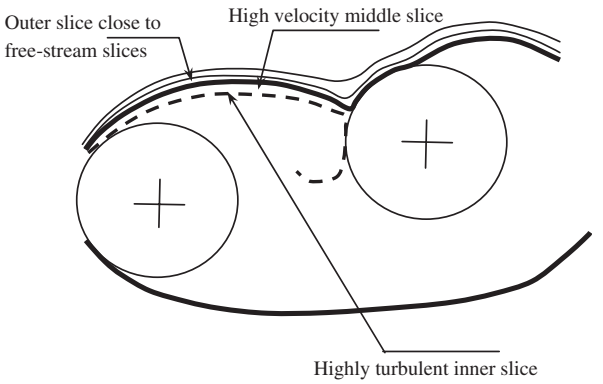

Fig. 2. A schematic diagram of shear layer reattachment.

2. Experimental details

Fig. 1 is a schematic diagram showing the arrangement of two cylinders, definition of symbols and coordinate systems. The stagger angle α is defined as the angle between the free-stream flow and the line connecting the centers of the two cylinders. The position of a point on the surface of a cylinder is defined by the azimuthal angle θ, measured from the direction of the free-stream flow. The angle θ is considered to be positive (0–180°) for the outer surfaces and negative (0° to −80°) for the inner surfaces of the cylinders. T is the gap width between the cylinders, as opposed to center-to-center spacing adopted by other researchers. In this study, the repulsive (outward-directed) lift force is considered to be positive and attractive (inward-directed) lift force is considered to be negative.

2.1. Wind tunnel

The experiments were conducted in a closed-circuit wind tunnel with a test-section of 300 mm in width, 1200 mm in height and 2200 mm long. The cylinders used as the test models, made of brass, each 49 mm in diameter, spanned the horizontal 300 mm dimension of the test-section. The free-stream velocity, U_0, in the test-section was 17 m/s, giving a Reynolds number (Re) of 5.5×10^4, based on the free-stream velocity and the diameter of a cylinder. Within the central area of 240 mm × 950 mm of the test-section, the flow was uniform within ±2% of the center-line velocity, and the longitudinal turbulence intensity was less than 0.5% in the absence of the cylinders. Circumferential time-averaged and fluctuating pressures on the surface of an isolated cylinder were measured at $z = 0$ (mid-span), and ±35 and ±80 mm in order to check the spanwise uniformity and separation of the flow on the circular cylinder, as well as fluid forces being measured by a load cell (which will be discussed in the next subsection). The results showed that the time-averaged and fluctuating pressure distributions at the five different sections were the same within experimental uncertainties. The overall uncertainties in time-averaged pressure, fluctuating pressure, time-averaged drag, fluctuating drag and fluctuating lift measurements were estimated to be ±2%, ±3%, 2%, 4% and 3.5%, respectively. The geometric blockage and the aspect ratios per cylinder at the test-section were 4% and 6, respectively. Effects of such blockage and aspect ratio on time-averaged and fluctuating fluid force coefficients of an isolated cylinder have been discussed in Alam et al. (2003a). No corrections were made to compensate the blockage effect because of difficulties related to flow interference between the two cylinders.

2.2. Fluid force and pressure measurements

Fluid forces were measured for a small span of the cylinders by a direct measurement method. As shown in Fig. 3, the cylinder on which measurements were conducted consisted of two parts: an active ('live') section and a dummy section, each being fitted with a load cell that consisted of four semiconductor strain gauges. The active section corresponded to mid-span of the cylinder. The load cell inside the active section measured a combination of fluid forces and forces due to vibration transmitted from the outside through the cylinder support, while that inside the dummy section measured the latter forces only. Hence, the fluid forces acting on the active section could be calculated by subtracting the output of the load cell inside the dummy section from that of the load cell inside the active section. The spanwise size of the active section was 45 mm (0.92 times the diameter of the cylinder). This size was determined taking into account the spanwise cross-correlation length of the fluctuating pressure. The details of the load cells and fluid force measurement have been described by Sakamoto and Oiwake (1984) and Sakamoto et al. (1994).

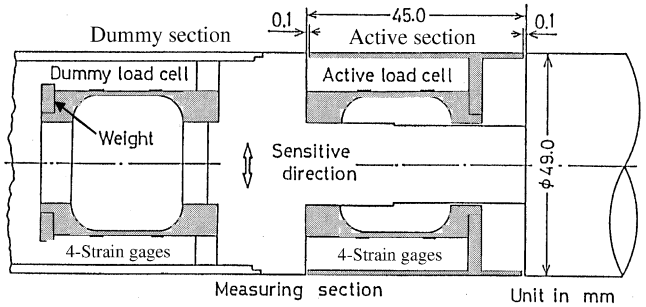

Fig. 3. Installation of load cells inside a cylinder.

Four test cylinders of the same diameter and length were used for the wind tunnel experiment. One was built with load cells for the measurement of fluid forces, one was a dummy cylinder, and the other two were used to measure surface pressure. One of the two comprised a semiconductor pressure transducer at mid-span (Fig. 4(a)) and the other included two parts, each part comprising a semiconductor pressure transducer with a tap opening (Fig. 4(b)). This cylinder was constructed such that one part of it can be rotated with respect to the other. The gap between the pressure tap openings of this cylinder was 6 mm. This cylinder was used for measuring surface pressure of the cylinders in the so-called switching or bistable flow region. In the bistable flow region, the angular position of a pressure tap opening was fixed at an azimuthal angle at which the difference in the pressure coefficient between the two stable flow states is the greatest, and the other pressure tap opening position was rotated with 10° interval. The outputs from both transducers were stored simultaneously and the signal from the fixed pressure tap was used as the reference signal to decompose the other signal for the two stable flow states. The details of the decomposition have been described by Alam et al. (2003a).

The pressure transducers were set just below the surface of the cylinders and communicated to the surface through pressure connections of 0.8 mm diameter and 1.5 mm long, as shown in Fig. 4(a). Each cylinder fitted with pressure tapping could be rotated, so as to measure the pressure distribution around 360°. A protractor was fixed concentrically at one end of the cylinder outside the wind tunnel and a pointer was attached to wall, thus enabling the incidence of the pressure tap to be determined. The dynamic response of the transducers was from 0 to 550 Hz. The transducers responded reasonably well to the pressure fluctuations up to 500 Hz with a gain factor of 1 ± 0.06, with a negligible phase lag. This frequency was well above the frequency of vortex shedding from the cylinders.

2.3. Flow visualization

Flow visualization was carried out in a water channel with a 1500 mm long rectangular working section (250 mm × 350 mm). A fine-mesh honeycomb was used to remove any large-scale irregularities. Two circular tubes with identical diameter of 20 mm were used. The flow visualization test in the water channel was conducted at a Reynolds

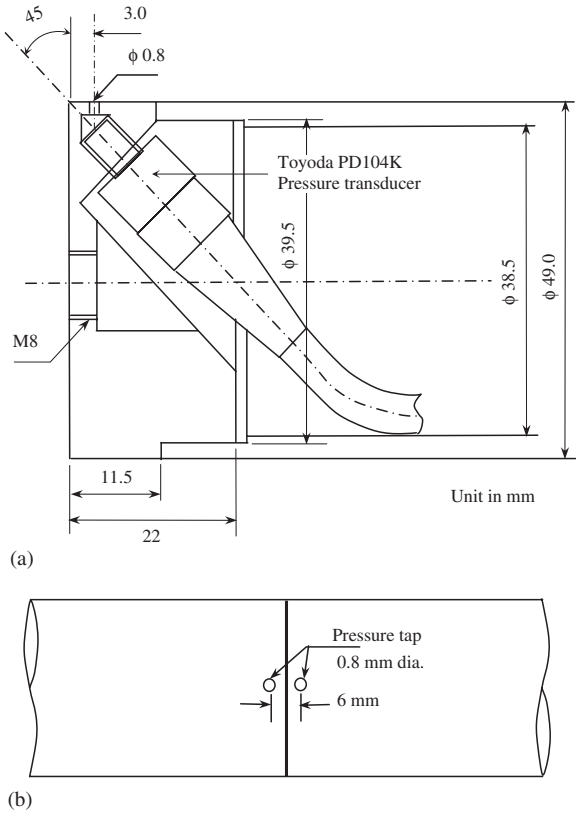

Fig. 4. (a) Installation of a pressure transducer inside a cylinder, and (b) location of two pressure taps under which two pressure transducers are installed in the same way as in (a).

number of 350. This Reynolds number is beyond the transition range to turbulence in the wake, as fully turbulent shedding conditions prevail for $Re > 300$ (Williamson, 1996). A platinum wire of 0.02 mm in diameter was used to generate hydrogen bubbles for flow visualization. The blockage and aspect ratio per cylinder at the test-section of the water channel were 4% and 13%, respectively.

2.4. Surface oil-flow visualization

The surface oil-film technique was used to visualize the flow pattern on the cylinder surface in order to obtain information on the reattachment and separation positions of the flow. The cylinders were wrapped with a black film of 0.03 mm in thickness, and then an even coating of a solution containing silicone oil, titanium dioxide, oleic acid and kerosene at a ratio of 45:3:2:2 in weight was painted on the surface. The solution distribution on the cylinder surface was achieved after at least 15 min of exposure to the uniform flow in the wind tunnel. The black film was then unwrapped carefully, and photographs of the solution distribution on the film were taken with a digital camera. Surface oil-flow visualizations were performed at the same Reynolds number as the measurements of fluid force and pressure. The experimental uncertainty in angular position of shear layer separation or of reattachment position obtained from surface oil-film techniques was estimated to be $\pm 1^\circ$.

2.5. Choice of Reynolds numbers

Higher subcritical Reynolds numbers are commonly found in many engineering applications (Sumner et al., 2000). Furthermore, fluctuating fluid forces acting on a circular cylinder at the higher subcritical Reynolds number range are significantly high and are comparatively insensitive to a change in Reynolds number in the range of $Re = 3 \times 10^4$–2×10^5 (Zdravkovich, 1997; Norberg, 2003), in which the wake and the shear layers of the cylinder are turbulent but the boundary layers are laminar (Zdravkovich, 1997). So, a Reynolds number of 5.5×10^4 in the higher subcritical range was chosen for the wind tunnel tests. However, flow visualization tests at such a high Reynolds number were not possible in our experimental facilities. Also, flow visualization pictures taken at a low Reynolds number are of better quality to clearly show the behaviors of the shear layers, vortex dynamics and interactions of vortices on a surface of a cylinder. Hence, a lower Reynolds number was chosen for the flow visualization tests in the water channel. It is known that the wake behind a circular cylinder firstly becomes turbulent in the range of $Re = 180$–400 and the shear layers are still laminar. The Reynolds number for the flow visualization tests was chosen as $Re = 350$. It is expected that the flow visualization results obtained at the Reynolds number of 350 can be compared only qualitatively with the results obtained at $Re = 5.5 \times 10^4$ chosen for the wind tunnel tests, as at least the wake for both cases is turbulent. However, great caution is obligatory when the results obtained at $Re = 5.5 \times 10^4$ (wind-tunnel tests) are discussed in relation to flow visualization patterns taken at $Re = 350$.

3. Results and discussion

3.1. Tandem ($\alpha = 0^\circ$) and side-by-side ($\alpha = 90^\circ$) arrangements

The well-known critical geometries of two cylinders are the tandem and side-by-side arrangements. The tandem arrangement is the critical geometry between staggered configurations of $\alpha = 0^\circ+$ and $0^\circ-$ (Sumner et al., 2000). On the other hand, the side-by-side arrangement is the critical geometry between staggered configurations of $\alpha = 90^\circ-$ and $\alpha = 90^\circ+$ (Kiya et al., 1980; Alam and Sakamoto, 2005). Extensive measurement results of time-averaged and fluctuating fluid forces, time-averaged and fluctuating surface pressures, Strouhal numbers and flow configuration of two circular cylinders in side-by-side and tandem arrangements have been presented by the present authors in Alam et al. (2003a–c).

3.2. Staggered arrangement with $\alpha = 10^\circ$

Since the case of $\alpha = 10^\circ$ is slightly staggered from the in-line configuration, there may be some similar characteristics of the flow at $\alpha = 10^\circ$ to those for the tandem and, of course, the change in the configuration will cause some new characteristics of the flow on the two cylinders. At $\alpha = 10^\circ$, $T/D < 1.3$, a bistable flow over the two cylinders was observed, i.e., two modes of the flow structure occurred intermittently and switched from one to the other. Each mode was sufficiently stable as was observed in fluid force signals. A typical lift force signal of the downstream cylinder at

$T/D = 0.10$ is shown in Fig. 5. It is clear from the signal that there are two modes of the lift force corresponding to two modes of the flow pattern. The flow mode that corresponds to the higher magnitude of the lift force is denoted as mode 1 and the flow mode that corresponds to the lower magnitude is denoted as mode 2 for future reference. Also, wavelet scalograms (not shown) of the signal (Fig. 5) demonstrated convincingly that modes 1 and 2 correspond to Strouhal numbers of 0.47 and 0.09, respectively (Alam and Sakamoto, 2005).

In order to elucidate the two modes of the flow responsible for the bistability, the time-averaged pressure coefficient, C_P, as well as the fluctuating pressure coefficient, C_P', on the surface of the downstream cylinder were calculated for the two modes by employing a conditional sampling technique (Alam et al., 2003a) on digitally stored composite signals. C_P and C_P' distributions for the two modes of the flow pattern at $T/D = 1.0$ are shown in Fig. 6. It is seen that C_P attains a value of unity at $\theta = 30^\circ$, i.e., the stagnation point, for both modes. Both C_P and C_P' distributions indicate that the outer shear layer separates from the downstream cylinder at the same position, irrespective of the flow modes; however, the inner shear layer separates at $\theta = -70^\circ$ and -30° for modes 1 and 2, respectively (Batham, 1973; Alam et al., 2003c). That is, the inner shear layer of the downstream cylinder sweeps on the surface of the downstream cylinder for a longer peripheral length for mode 1, thus creating a higher suction pressure before separation. Mode 1 exhibits a longer pressure recovery region on the inside surface, indicating the occurrence of the inner shear layer reattachment, which is confirmed by the surface oil-flow visualization pattern on the downstream cylinder. It was found that, as the stagger angle of the cylinders was slightly increased or decreased, say at $\alpha = 8^\circ$, mode 1 only was observed, and at $\alpha = 12^\circ$, mode 2 only was observed. The C_P and C_P' distributions at $\alpha = 8^\circ$ and 12° ($T/D = 1.0$) are shown in Fig. 7. The trends of the pressure distributions for $\alpha = 8^\circ$ and 12° bear resemblance to with those of the modes 1 and 2 (Fig. 6), respectively.

Now, a summary sketch of the flow pattern based on the C_P and C_P' distributions and surface oil-flow patterns can be presented in Fig. 8. In mode 1, as evident in the surface oil-flow pattern ($\alpha = 8^\circ$, Fig. 8(a, c)), the inner shear layer separating from the upstream cylinder reattaches onto the downstream cylinder at $\theta = 31^\circ$, and the gap shear layer consisting of the high velocity middle slice and the highly turbulent inner slice sweeps on the inner surface and separates at $\theta = -58^\circ$, followed by a turbulent reattachment at $\theta = -65^\circ$. The reattached shear layer finally separates at $\theta = -108^\circ$. As the high velocity middle slice reattaches on the inside surface and sweeps on a longer peripheral length, the region of a high suction pressure is created before the final separation.

In mode 2 ($\alpha = 12^\circ$), the inner shear layer from the upstream cylinder reattaches onto the downstream cylinder at $\theta = 27^\circ$, and the gap shear layer (the inner shear layer around the downstream cylinder) consisting of outer slice, high velocity middle slice and highly turbulent inner slice, passes through the gap and separates at $\theta = -41^\circ$. Interestingly, the separation position inferred from surface oil-flow patterns coincides with the position of the peak in the C_P' distributions, i.e., a peak in C_P' distribution occurs in the vicinity of the separation point of a shear layer. It can be mentioned that, as the gap shear layer of mode 1 is more turbulent than that of mode 2, the gap shear layer is induced to reattach. Modes 1 and 2 discussed here are consistent with the flow patterns II_B and III_B, respectively. Gu and Sun (1999) observed at $Re = 2.2 \times 10^5$ two ranges of the critical staggered angle at which the flow patterns II_B and III_B switched from one to the other. The critical ranges of the stagger angle were $\alpha = 10$–16° at $T/D < 1.2$ and $\alpha = 16$–25° at $T/D = 2.0$. They further observed that the critical stagger angle increased with change in Reynolds number. Also, the critical stagger angle is supposed to be a function of the free-stream turbulent intensity and Reynolds number. The presently observed critical stagger angle is 10°, slightly below the range observed by Gu and Sun (1999). This is probably because of the difference in Reynolds numbers and of the difference in turbulent intensities. The turbulent intensity was 0.5% at $Re = 5.5 \times 10^4$ but was 0.2% at $Re = 2.2 \times 10^5$ in Gu and Sun's (1999) measurements.

It has been mentioned that the gap shear layer of the downstream cylinder separates at $\theta = -58^\circ$ and -41° for $\alpha = 8^\circ$ and 12°, respectively (Fig. 8). However, in Fig. 7(a), it is seen that the pressure recovery starting point (minimum pressure point) is at about -30° and -20° for $\alpha = 8^\circ$ and 12°, respectively. That is, the separation point is quite far away from the pressure recovery starting point. It is known that the pressure recovery region becomes shorter for a laminar separation and becomes longer for a turbulent separation or for Re larger than the critical (Zdravkovich, 1997). This is indeed reconfirmed presently. The pressure recovery region on the outside surface is shorter because the outer shear layer, which is close to the free-stream, is associated with laminar separation but longer on the inside surface because the gap flow is highly turbulent. It is also known that the laminar separation point of a shear layer is 5–10° from the pressure recovery starting point. This distance increases for a turbulent shear layer, and the increase depends on the turbulence level (Alam, 2004). In our case, the gap shear layer around the downstream cylinder is highly turbulent, resulting in a longer pressure recovery region and increased remoteness of the flow separation point from the pressure recovery starting point.

For mode 2, although C_P varies monotonically between $\theta = 30^\circ$ (stagnation point) and $\theta = -30^\circ$ for both $\alpha = 12^\circ$ and 10°, a peak in each of the C_P' distributions occurs at $\theta = 10^\circ$, i.e., the position of the peak is about 20° forward from the stagnation point. Such a peak was observed for mode 2 at other T/D values (< 1.3) also. The significance of the

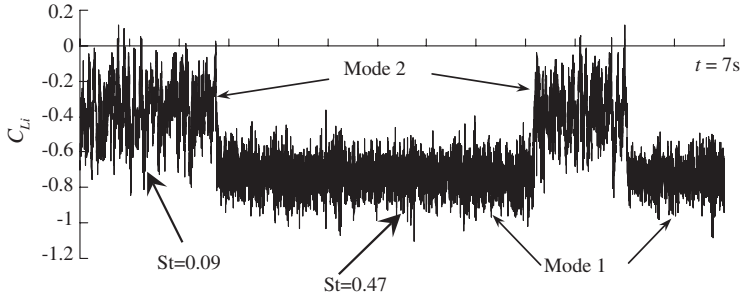

Fig. 5. Lift force signal showing a bistable flow for $T/D = 0.10^{\circ}$, $\alpha = 10^{\circ}$.

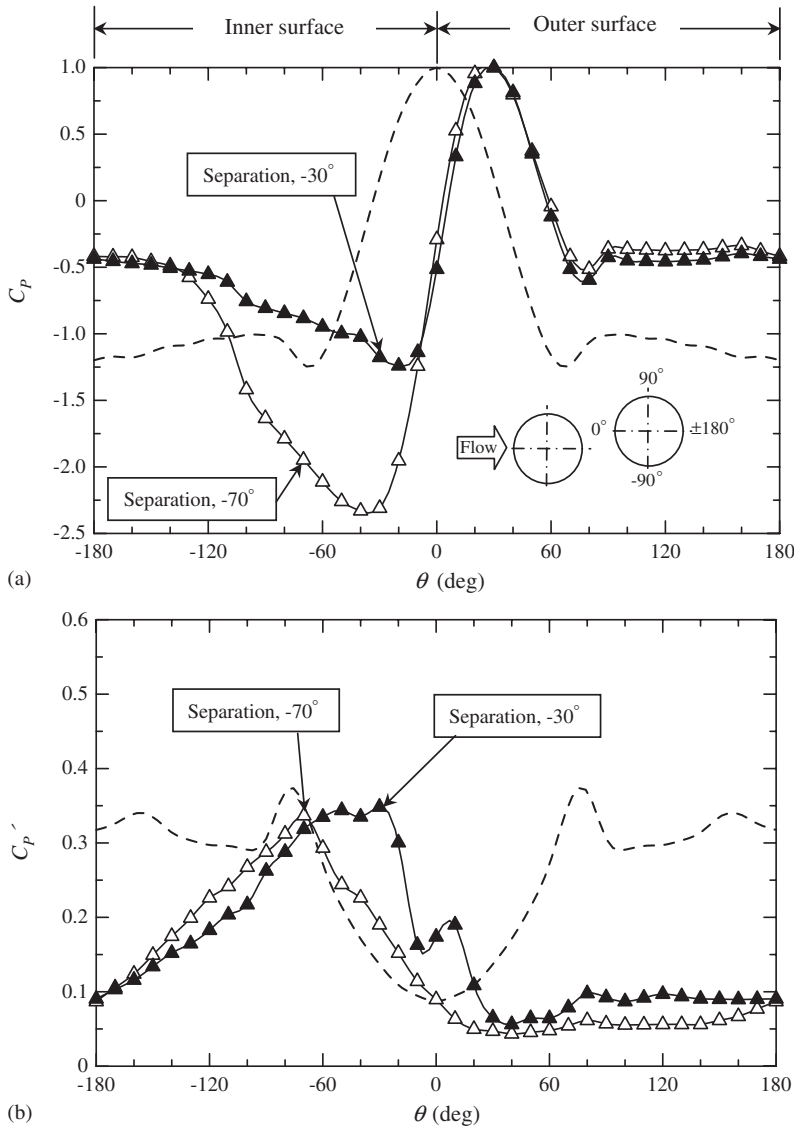

Fig. 6. $T/D = 1.0$, $\alpha = 10^{\circ}$, downstream cylinder: (a) time-averaged pressure coefficient, C_P, distribution, (b) fluctuating pressure coefficient, C_P', distribution; △, mode 1; ▲, mode 2; - - -, single cylinder.

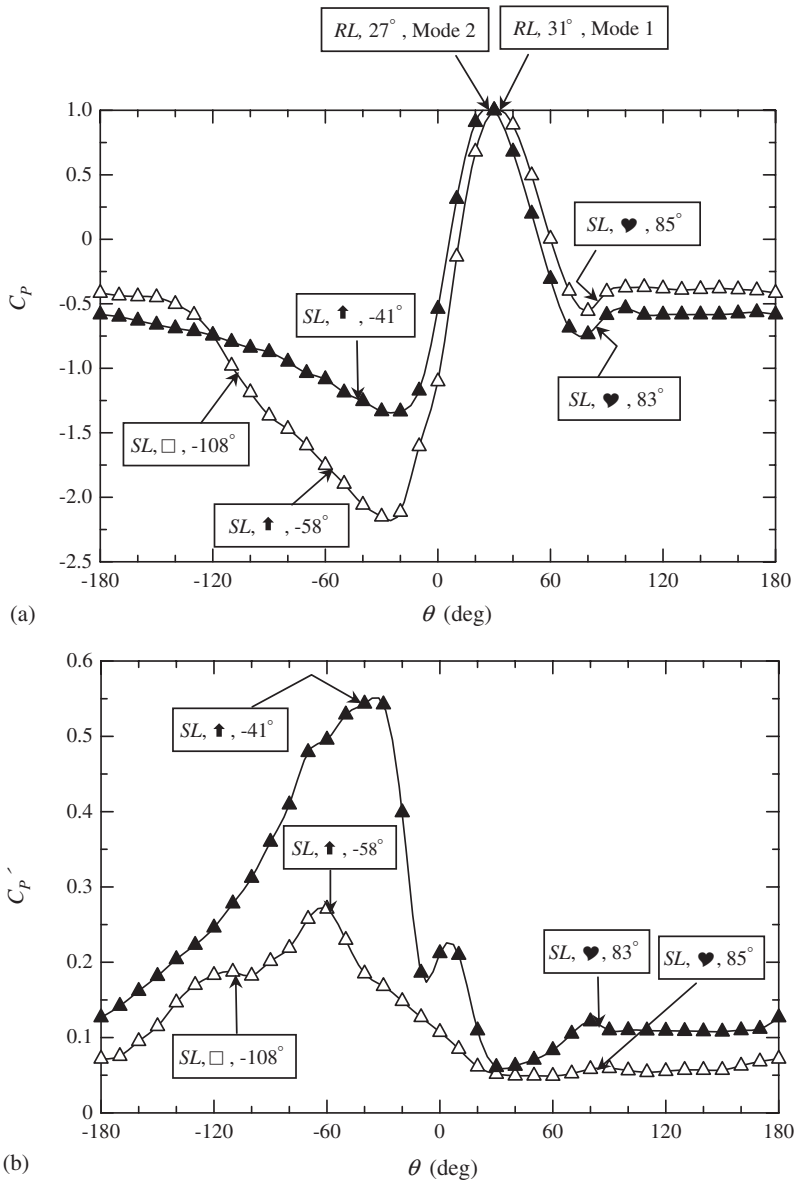

Fig. 7. $T/D = 1.0$, downstream cylinder: (a) time-averaged pressure coefficient, C_P, distribution, (b) fluctuating pressure coefficient, C_P', distribution; △, $\alpha = 8^\circ$;▲, $\alpha = 12^\circ$. See Fig. 8 for the definition of other symbols.

appearance of the peak near the stagnation point is unknown. It is however not reflected on the surface oil-flow patterns.

The flow pattern around the two cylinders at $T/D = 0.10$ is rather different from that at $T/D = 1.0$, mainly due to a difference in the characteristics of the flow on the upstream cylinder. Sketches of the two modes of the flow pattern at $T/D = 0.10$ are shown in Fig. 9. The flow pattern around the downstream cylinder at $T/D = 0.10$ is almost the same as that at $T/D = 1.0$, regardless of the mode; however, the flow pattern around the upstream cylinder is quite different for $T/D = 0.10$ and 1.0. Because of the very small gap between the cylinders at $T/D = 0.10$, part of the reverse flow from the front surface of the downstream cylinder reattaches again onto the rear surface of the upstream cylinder, forming a separation bubble on the inner side surface of the upstream cylinder, as seen in the figure. The reattachment of the reverse flow is quite steady and a quasi-steady vortex region is formed beneath the inner shear layer of the upstream cylinder. Such reattachment of the reverse flow was also observed in the case of two tandem cylinders at $T/D = 0.10$

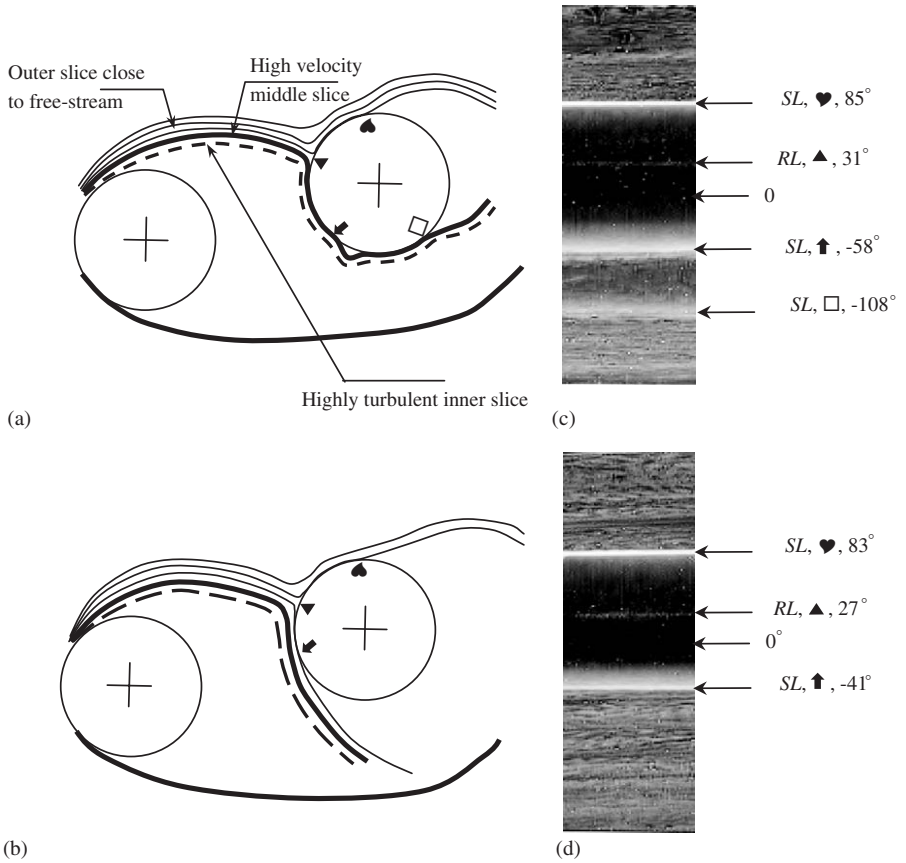

Fig. 8. Sketches and surface oil-flow patterns: (a) mode 1, (b) mode 2, (c) oil-flow pattern on downstream cylinder for $\alpha = 8^\circ$, $T/D = 1.0$, (d) oil-flow pattern on downstream cylinder for $\alpha = 12^\circ$, $T/D = 1.0$; SL = separation line, RL = reattachment line.

(Alam et al., 2003c). The flow pattern sketched in Fig. 9 is well supported by the C_P and C_P' distributions around the upstream cylinder in Fig. 10 and around the downstream cylinder (not shown). In Fig. 10(a), the peaks at $\theta = -150^\circ$ and -155° in the C_P distributions for modes 1 and 2, respectively, result from the reattachment of the reverse flow. The very small pressure fluctuation at the region of $\theta = 0^\circ$ to -120° (Fig. 10(b)) indicates an extremely steady inner shear layer of the upstream cylinder and the flow in the quasi-steady vortex region. Also, it is evident in Figs. 7 and 10 that mode 1, in which a turbulent reattachment follows the laminar separation of the inner shear layer from the downstream cylinder, is associated with a smaller fluctuation of pressure on the surfaces of the two cylinders than mode 2.

The time-averaged drag coefficient, C_D, time-averaged lift coefficient, C_L, fluctuating (r.m.s.) drag coefficient, C_D', and fluctuating (r.m.s.) lift coefficient, C_L', of the upstream and downstream cylinders are shown in Fig. 11 as a function of T/D. Since two modes of the flow pattern have been demonstrated for $T/D < 1.3$, two sets of fluid force coefficient values for each cylinder are given in the figure. The range of $T/D = 0.1$–1.3 is hereinafter referred to as bistable flow region I. The trends of the C_D distributions of the upstream and downstream cylinders in mode 1 resemble with those of two cylinders in the tandem arrangement (Zdravkovich and Pridden, 1977; Igarashi, 1981; Alam et al., 2003c). For example, the downstream cylinder experiences negative drag for $T/D < 2.1$, and the drag force acting on the upstream cylinder decreases gradually with increasing T/D. Compared with mode 2, mode 1 induces a large positive drag on the upstream cylinder and a negative drag of large magnitude on the downstream cylinder, because of the development of a high suction pressure on the front quadrant of the inner surface of the downstream cylinder (Fig. 6). An interesting feature of mode 1 is that it induces a negative lift force of large magnitude ($C_L = -1.22$) on the downstream cylinder at $T/D = 1.0$ (Fig. 11(b)). The range of $T/D = 0.4$–1.4 coincides with the so-called '*inner negative lift peak*' region in the contour map of C_L in the T/D versus α plane. The corresponding pressure distribution responsible for such a higher magnitude of negative C_L has already been shown in Fig. 6(a). The C_L obtained by from integrating the pressure distribution shown in Fig. 6(a) was evaluated to be -1.23. The pressure distribution (Fig. 6(a)) implies that the higher

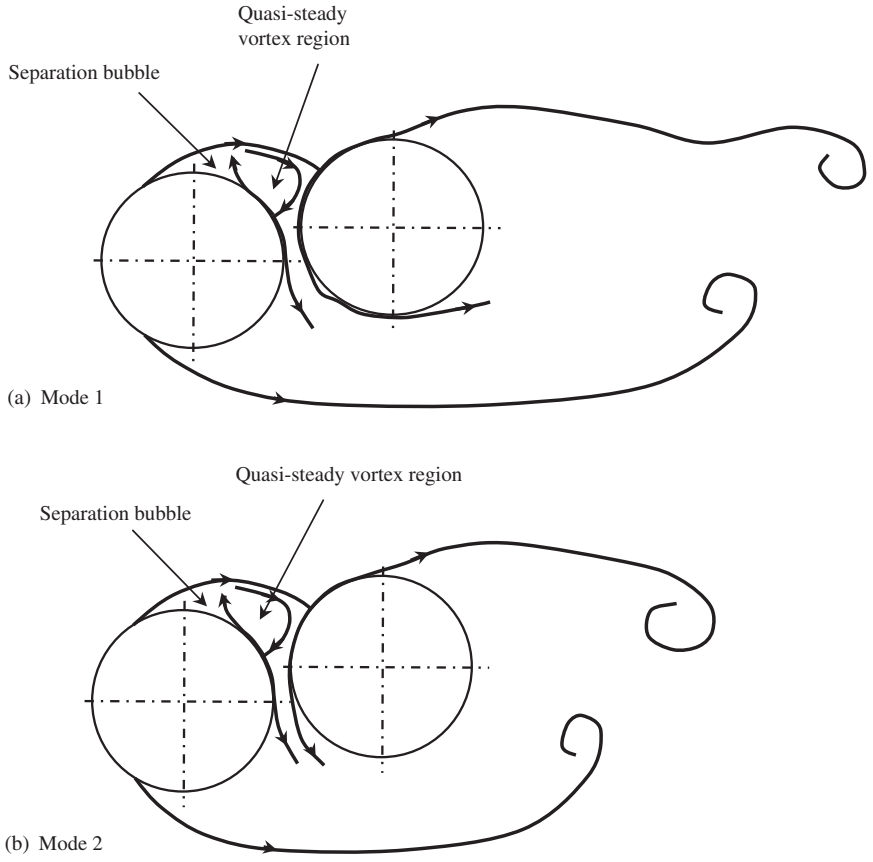

Fig. 9. Sketches of two modes of flow at $T/D = 0.10$, $\alpha = 10^\circ$.

magnitude of C_L at $T/D = 1.0$ in Fig. 11(b) is mostly contributed from the highly negative (suction) pressure induced by the inner shear layer that contains the high velocity middle slice of the shear layer of the upstream cylinder. The highly negative value of C_L can be further explained in terms of circulation, i.e., the high velocity middle slice sweeping over the inner surface of the downstream cylinder for a longer peripheral length causes a large anticlockwise circulation, resulting in a highly negative (downward, in reference to Fig. 1 or 8) lift force on the downstream cylinder. However, Zdravkovich and Pridden (1977), Zdravkovich (1987) and Ting et al. (1998) ascribed this negative lift force to a flow condition in which most of the fluid approaching the downstream cylinder passed through the gap between the cylinders. The present study presents a more comprehensive explanation of the cause of the negative lift force acting on the downstream cylinder. Here our conclusion on the cause of negative force is that the negative lift is due not only to the shift of the stagnation point toward the outer side but also to the high velocity middle slice sweeping over the inner surface of the downstream cylinder for an extended peripheral length (Figs. 7 and 8). Such a highly negative lift was also found for a circular cylinder located behind a blunt-based flat plate, with longitudinal spacing of $1.0D$ and transverse spacing of $0.25D$ from the base of the flat plate (Keser and Unal, 2003). It implies that the lift force of large magnitude on the downstream cylinder is not so sensitive to the cross-section of the upstream body.

Mode 1 remains evident for $T/D = 1.3$–2.1 when mode 2 disappears. The disappearance of mode 2 for $T/D = 1.3$–2.1 is also supported by the results obtained by Gu and Sun (1999); but the observation is contradictory to Zdravkovich's (1987) report that the bistable flow occurred for a constant transverse spacing between the cylinders, implying the presence of mode 2 ($\alpha = 10^\circ$) at $T/D = 1.3$–2.1, which is just the reverse of the present case. In order to corroborate which flow pattern appears in the range of $T/D = 1.3$–2.1, time-averaged and fluctuating pressures on the surface of the downstream cylinder were measured at $T/D = 1.8$, and they appeared similar to those of mode 1 at $T/D < 1$, implying the existence of mode 1 at $T/D = 1.3$–2.1. Further, the stored lift force signals suggested that, at $T/D = 0.10$, the existence of modes 1 and 2 were approximately 50% each of the total time; on the other hand, as T/D increased from 0.1 to 1.3, the occurrence of mode 2 is less likely than that of mode 1, which is consistent with the sole presence of mode 1 at $T/D = 1.3$–2.1.

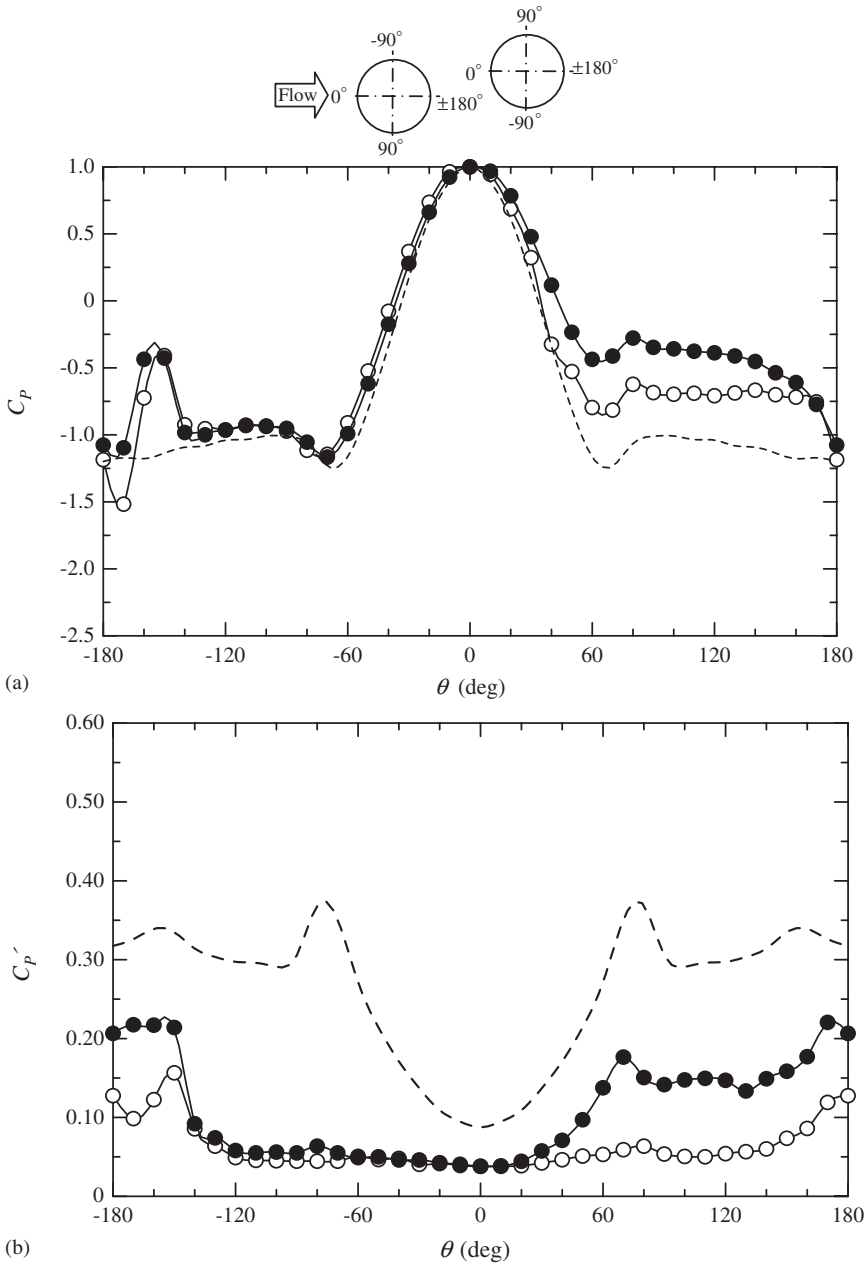

Fig. 10. Time-averaged and fluctuating pressure coefficient distributions on the surface of upstream cylinder for $T/D = 0.1$, $\alpha = 10°$: (a) C_P, (b) C_P'; ○, mode 1; ●, mode 2; - - -, single cylinder.

It is seen that mode 2 corresponds to larger fluctuating fluid forces (C_D' and C_L') but smaller C_D on both cylinders than mode 1. At $T/D = 0.1$–2.1, the values of C_D' and C_L' of the upstream cylinder are very low and decrease gradually with increase in T/D; however, those of the downstream cylinder increase gradually. This implies that, as the spacing increases from 0.1 to 2.1, the steadiness for the flow over the upstream cylinder is improved gradually, but the flow over the downstream cylinder becomes more unsteady to shed stronger vortices. The range of $2.1 < T/D < 2.4$, marked by a shadow, is another bistable flow region, where the fluid force coefficients (C_D, C_L, C_D' and C_L') of both cylinders jump from a small to a large value. This region is identified as bistable flow region II. In this bistable flow region, the jump in the fluid forces is apparently due to a switch in the flow structure from one type to another. The switch in the flow was

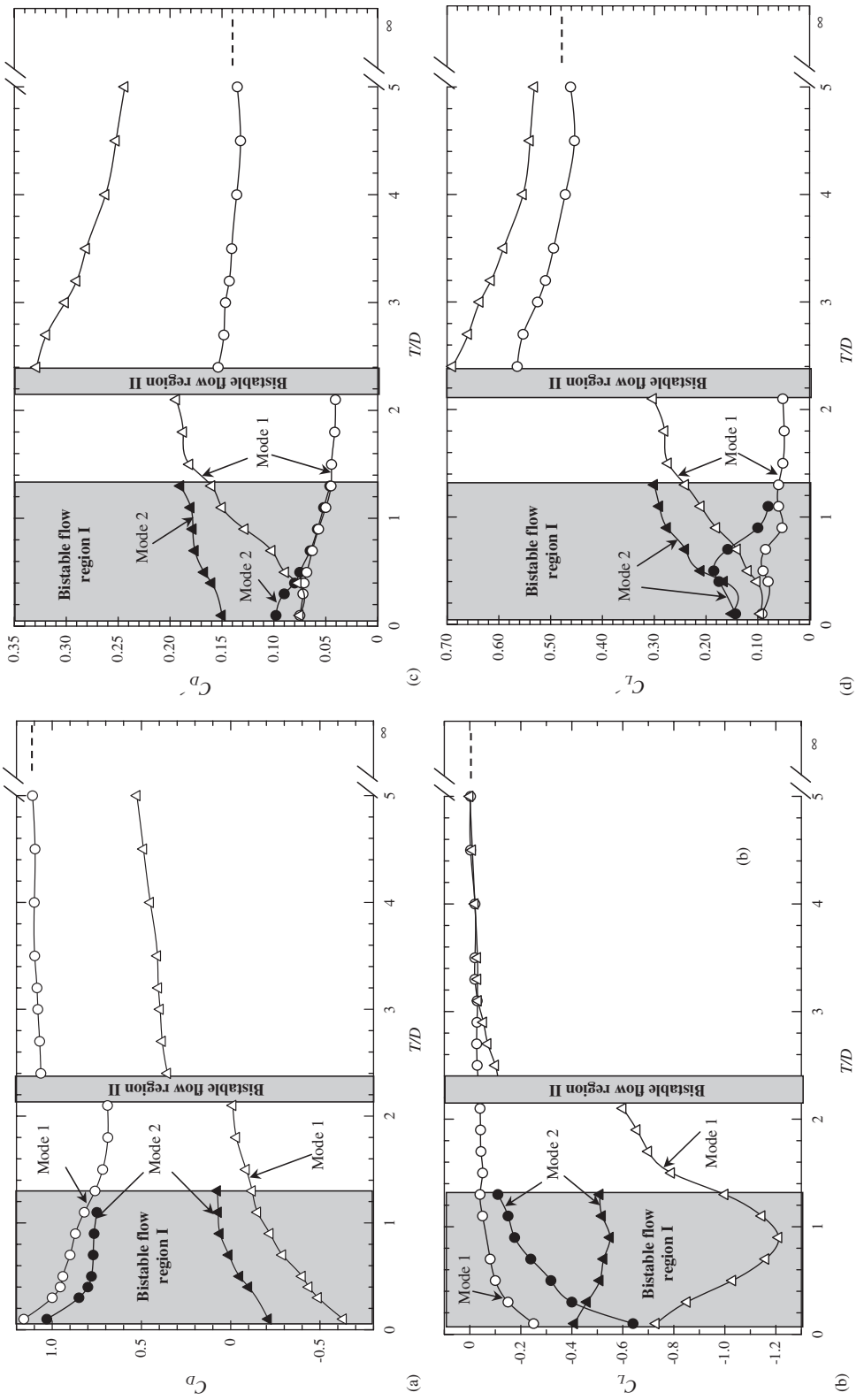

Fig. 11. Fluid force coefficient distributions at $\alpha = 10^\circ$: (a) C_D, (b) C_L, (c) C'_D, (d) C'_L; ○, ●, upstream cylinder; △, ▲, downstream cylinder; - - - single cylinder.

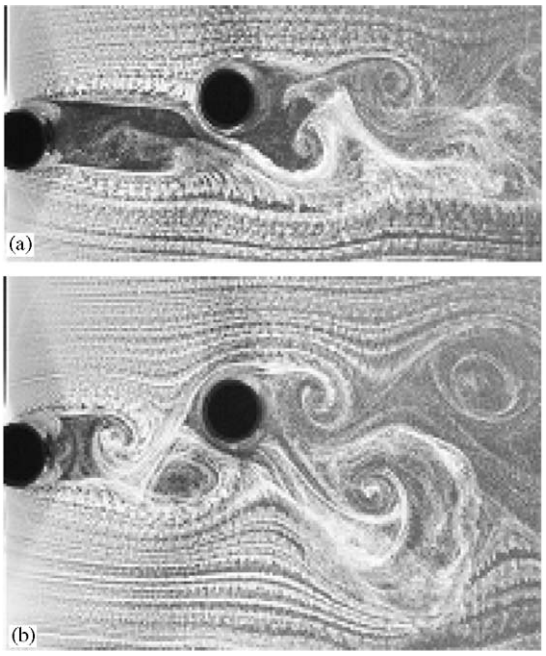

Fig. 12. Visualized bistable flow patterns at $T/D = 2.5$, $\alpha = 10^\circ$: (a) reattachment flow, (b) fully developed Karman vortex flow behind the upstream cylinder. These flow patterns should correspond to those for $2.1 < T/D < 2.4$ (bistable flow region II) in the wind-tunnel tests.

also found in the flow visualization test. However, in the flow visualization test ($\mathrm{Re} = 350$), two totally different flow patterns and their switching were detected at $T/D = 2.5$ and the two flow patterns are shown in Fig. 12. The first flow pattern (Fig. 12(a)), reattachment flow, almost similar to mode 1, can be described as the pattern in which the inner shear layer of the upstream cylinder reattaches onto the downstream cylinder and part of the reattached flow sweeps over the inner surface of the downstream cylinder. In this mode, no Karman-type vortices are observed between the cylinders. Because of the low Reynolds number, the turbulent reattachment on the downstream cylinder following the laminar separation of the inner shear layer from the upstream cylinder is not expected to occur. On the other hand, in the second flow pattern (Fig. 12(b)), fully developed Karman-type vortices are observed behind the upstream cylinder and the flow over the downstream cylinder is enhanced significantly. This kind of bistable flow somehow resembles that observed in the case of two cylinders in tandem arrangement (Ishigai et al., 1972; Igarashi, 1981, 1984; Liu and Chen, 2002; Alam et al., 2002, 2003c). In the case of the tandem arrangement, the characteristics of the two flow patterns in the bistable flow region were: (i) for the first flow pattern, symmetrical steady reattachment of both shear layers of the upstream cylinder onto the downstream cylinder occurs and formation of Karman vortex between the cylinders is prevented, and (ii) for the second flow pattern, the two shear layers of the upstream cylinder form fully developed Karman vortices between the cylinders (Alam et al., 2002, 2003c). On the other hand, in the case of $\alpha = 10^\circ$, the characteristics of the two flow patterns in the region $2.1 < T/D < 2.4$ are: (i) for the first flow pattern, only the inner shear layer of the upstream cylinder reattaches steadily onto the downstream cylinder and formation of Karman vortex behind the upstream cylinder does not occur, and (ii) for the second flow pattern, fully developed Karman vortices are formed behind the upstream cylinder. Beyond the critical range of T/D, for $T/D = 2.4$–5.0, though C_D of the upstream cylinder (Fig. 11(a)) reaches that ($C_D = 1.12$) of an isolated cylinder, yet C_D of the downstream cylinder is smaller than that of the isolated cylinder, indicating that the downstream cylinder is still partially submerged in the wake of the upstream cylinder. Note that the values of C_D, C_D' and C_L' of a single, isolated cylinder were 1.12, 0.14 and 0.48, respectively. A comparison of these values with those obtained by other researchers has been presented in Alam et al. (2003a). At this range of T/D (2.4–5.0), the value of C_P on the surface of the downstream cylinder has never reached 1.0 (stagnation pressure), because the downstream cylinder is approached by the flow with large-scale vortices generated by the upstream cylinder. The flow shown in Fig. 12(b) also verifies the disappearance of the stagnation point on the downstream cylinder.

An interesting feature seen in Figs. 11(c, d) is that the values of C_D' and C_L' of the downstream cylinder as T/D just exceeds the bistable flow region II are extremely high. In order to acquire information about whether it is due to the

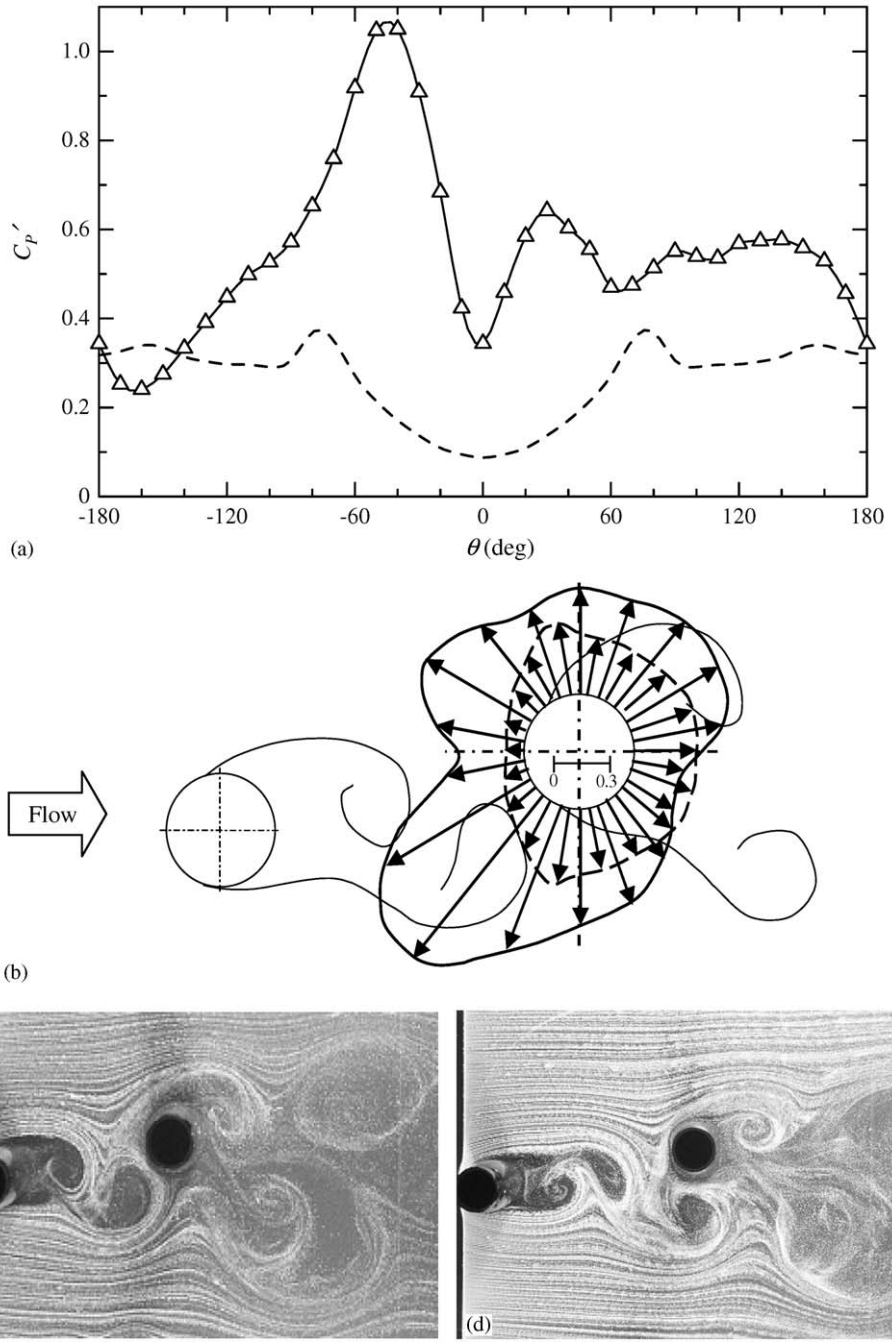

Fig. 13. Fluctuating (r.m.s.) pressure coefficient distribution on the surface of the downstream cylinder for $T/D = 2.6$, $\alpha = 10^\circ$: (a) in the Cartesian coordinate system, (b) in the polar coordinate system; - - -, single cylinder. (c, d) Visualized flow patterns: (c) $T/D = 2.8$, $\alpha = 10^\circ$; (d) $T/D = 4.0$, $\alpha = 10^\circ$.

wake of the downstream cylinder or due to the wake of the upstream cylinder, fluctuating (r.m.s.) pressure on the entire surface of the downstream cylinder was measured at $T/D = 2.6$ and is shown in Figs. 13(a, b). The figures show that significantly higher fluctuation of pressure occurs on the entire surface of the downstream cylinder, in comparison with that of a single, isolated cylinder; however, fluctuation of pressure is tremendously high, particularly on the front

quadrant of the inside surface, at $\theta = -10^\circ$ to -100°. The flow visualization pattern shown in Fig. 13(c) at $T/D = 2.8$ agrees well with the fluctuating pressure distribution at $T/D = 2.6$ in wind tunnel tests. As seen in the flow visualization pattern, the alternate strong rolling of the upstream cylinder vortices near the front quadrant of the inside surface of the downstream cylinder and impingement of the vortices on the surface during convection on the cylinder surface cause the tremendously high fluctuation of pressure at $\theta = -10^\circ$ to -100° of the downstream cylinder (Gursul and Rockwell, 1990; Tang and Rockwell, 1983). The value of C_{pf} at $\theta = 10$–170°, considerably greater than that of an isolated cylinder, indicates that enhanced vortex shedding from the outer surface of the downstream cylinder occurs. So, it may be concluded that the large values of C_D' and C_L' of the downstream cylinder are contributed not only from the downstream cylinder wake but also from the upstream cylinder wake. The inner vortices shed from the inside surface of the upstream cylinder were found to impinge on the inner surface of the downstream cylinder. An outer vortex from the outer surface of the upstream cylinder pairs with an inner vortex from the downstream cylinder, enveloping the inner vortex of the downstream cylinder by the outer vortex of the upstream cylinder. As evident in Figs. 13(c, d), the inner vortices shed from the upstream cylinder lose their identity when passing the downstream cylinder; therefore, a single vortex street forms behind the downstream cylinder. The observation shows a resemblance to the interaction of the oncoming two rows of vortices on an elliptical leading edge, with a small transverse offset of the edge with respect to a row of vortices, as investigated by Gursul and Rockwell (1990).

3.3. Staggered arrangement with $\alpha = 25^\circ$

Fig. 14 shows C_D and C_L distributions of the upstream and downstream cylinders at $\alpha = 25^\circ$. The trends of the C_D and C_L distributions at $\alpha = 25^\circ$ are quite different from those at $\alpha = 10^\circ$. C_D and C_L of the upstream cylinder approach to the values of a single, isolated cylinder when T/D reaches 5.0; however, C_D of the downstream cylinder is somewhat greater than that of a single, isolated cylinder in the range of $T/D = 3.5$–5.0. It will be discussed later that the latter observation is linked to enhanced vortex shedding from the downstream cylinder because of the synchronization of this vortex shedding with the incident vortices from the upstream cylinder.

For simplicity, the main features of C_D and C_L distributions are pointed out first, and then they will be discussed consecutively. The main features seen in the figure are: (i) C_L of the upstream cylinder drastically changes at $T/D = 0.10$–0.30 and jumps at $T/D = 0.30$–0.50 (bistable flow region I), (ii) at $1.9 < T/D < 2.1$ (bistable flow region II), C_D of the upstream cylinder and C_L of the downstream cylinder experience a jump, and (iii) C_L of the downstream cylinder is negative and large in magnitude at $T/D = 2.1$–4.0. The three aspects are further elaborated below:

(i) The first feature in Fig. 14 is that C_L of the upstream cylinder changes briskly from a value of 0.08 at $T/D = 0.1$ to the minimum, -1.03, at $T/D = 0.3$, and then to –0.065 at $T/D = 0.5$, whereas the corresponding C_D follows such a change pattern at $T/D = 0.10$–0.30. However, changes in C_D and C_L of the downstream cylinder are less evident in the same range of T/D. In order to elucidate the flow patterns which are responsible for the change in C_L, time-averaged pressure distributions of the upstream cylinder at $T/D = 0.10$, 0.30 and 0.50 and oil-flow visualization patterns along with sketches of the flow patterns are shown in Fig. 15. The trends of the C_P distributions at $T/D = 0.10$, 0.30 and 0.50 imply that the flow patterns at those spacings are quite different from one another. At $T/D = 0.10$, the pressure distribution is symmetric about the stagnation point at $\theta = -130$–130°, yet exhibits a peak at $\theta = -140^\circ$, which results from the laminar reattachment of part of the reversed flow separating from the front surface of the downstream cylinder (Fig. 15(b)). In view of the 10° increment in θ (Section 2.2), the exact location of the peak may slightly deviate from $\theta = -140^\circ$.

From the surface oil-flow patterns (Fig. 15(b)), it is evident that the outer and inner shear layers around the upstream cylinder separate at $\theta = 68^\circ$ and -80°, respectively, and the inner shear layer reattaches steadily onto the downstream cylinder at $\theta = 22^\circ$. The outer part of the reattached shear layer separates at $\theta = 82^\circ$, and part of the reverse flow reattaches again onto the rear surface at $\theta = -135^\circ$ of the upstream cylinder. Actually, the reverse flow in the gap between the inner side surface upstream cylinder and the front surface of the downstream cylinder is steady, resulting in a clear reattachment line on the rear surface of the upstream cylinder. It is worth mentioning that the inner shear layer around the downstream cylinder separates at $\theta = -26^\circ$.

At $T/D = 0.30$, at which the magnitude of the lift force acting on the upstream cylinder is maximum, a large area of suction (highly negative pressure) is developed on the inner side surface (Fig. 15(a)). In this case, the inner shear layer of the upstream cylinder completely passes through the gap and the flow rate through the gap is considerably greater than that at $T/D = 0.10$. The inner shear layer separating from the upstream cylinder at $\theta = -102^\circ$ reattaches again onto the rear surface at $\theta = -150^\circ$ and the adjacent shear layers separate at $\theta = -140^\circ$ and -165°, as suggested by the

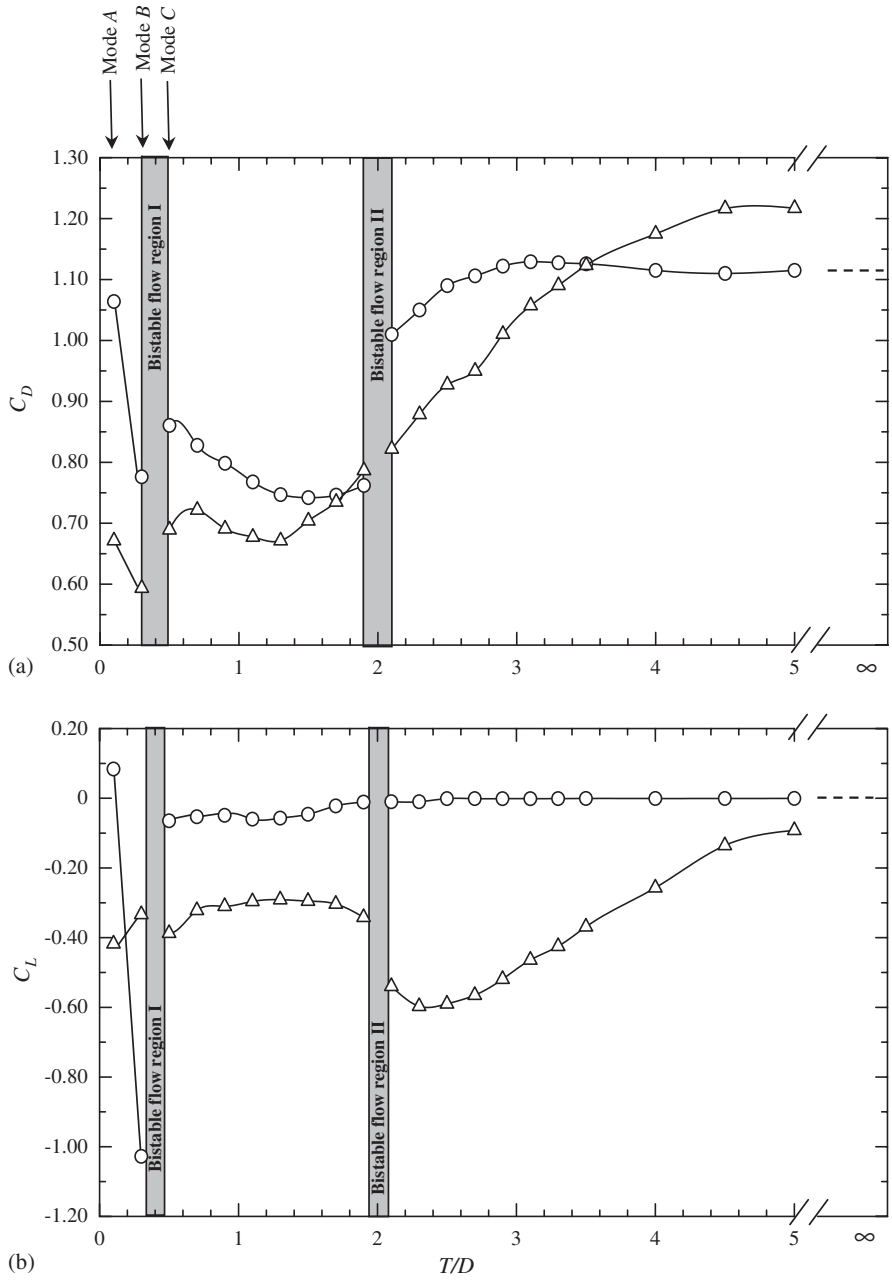

Fig. 14. Time-averaged drag and lift coefficient distributions at $\alpha = 25^{\circ}$: (a) C_D, (b) C_L; ○, upstream cylinder; △, downstream cylinder; ---, single cylinder.

separation bubble at $\theta = -102^{\circ}$ to -140° in Fig. 15(c). The longer pressure recovery region in the pressure distribution at $T/D = 0.30$ also suggests turbulent reattachment. Thus, the inner shear layer reattaching on the inside surface for a longer peripheral length causes a higher negative pressure on the inside surface as well as a greater magnitude of clockwise circulation around the upstream cylinder, resulting in the higher negative lift force acting on the upstream cylinder. At $T/D = 0.50$, the pressure distribution is almost symmetric about the stagnation point (Fig. 15(a)) and flow separation from the upstream cylinder occurs at -78° and 72° (Fig. 15(d)) for the inner and outer shear layers, respectively; i.e., flow over the upstream cylinder is similar to that of a single, isolated cylinder, at least in terms of the

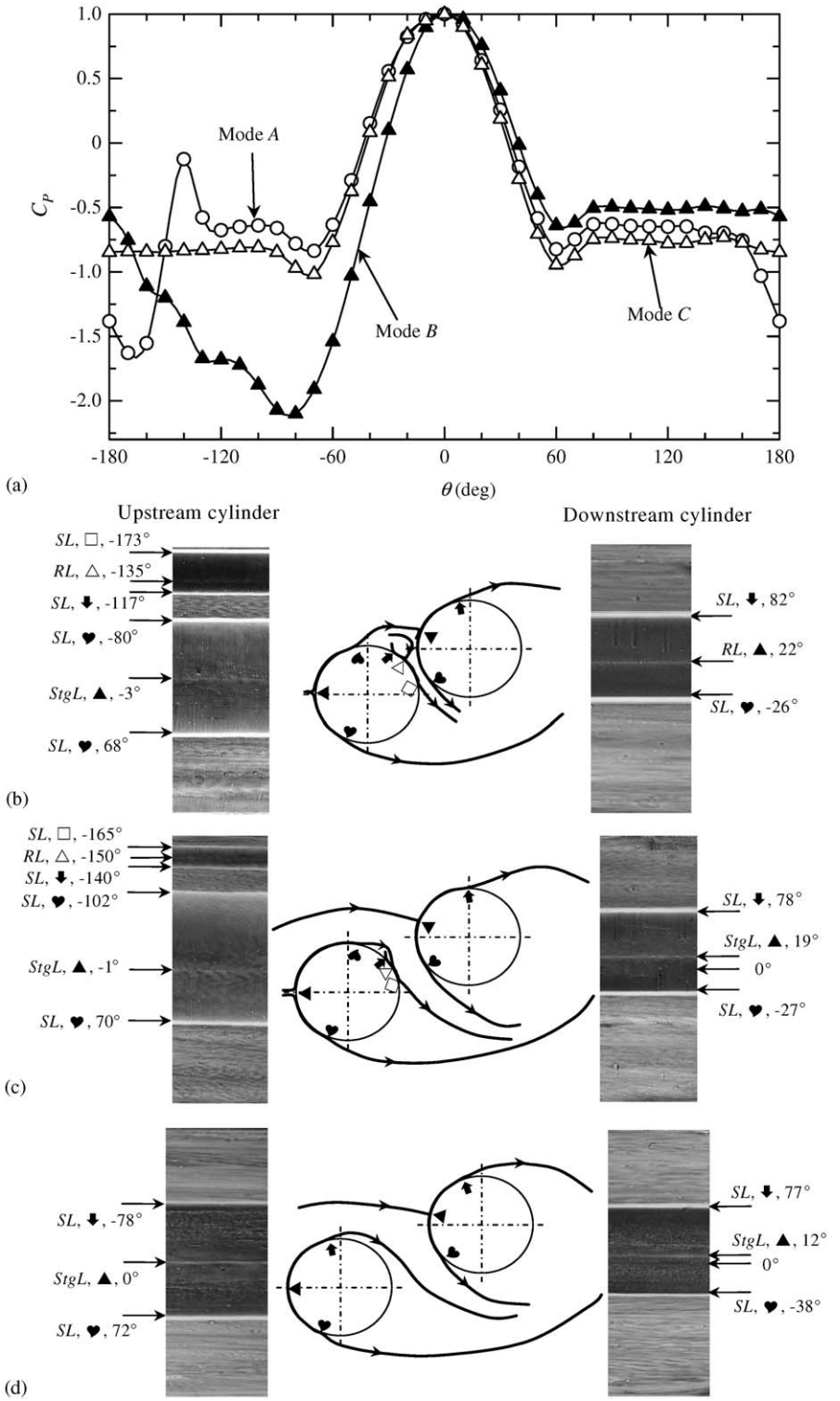

Fig. 15. (a) Time-averaged pressure coefficient distributions on the surface of the upstream cylinder at $\alpha = 25°$: ○, $T/D = 0.10$; ▲, $T/D = 0.30$; △, $T/D = 0.50$. (b, c, d) Surface oil-flow flow patterns and sketches of the flow patterns at $\alpha = 25°$: (b) $T/D = 0.10$, mode A; (c) $T/D = 0.30$, mode B; (d) $T/D = 0.50$, mode C. Left- and right-hand surface oil-flow patterns are for upstream and downstream cylinders, respectively. SL = separation line, RL = reattachment line, $StgL$ = stagnation line.

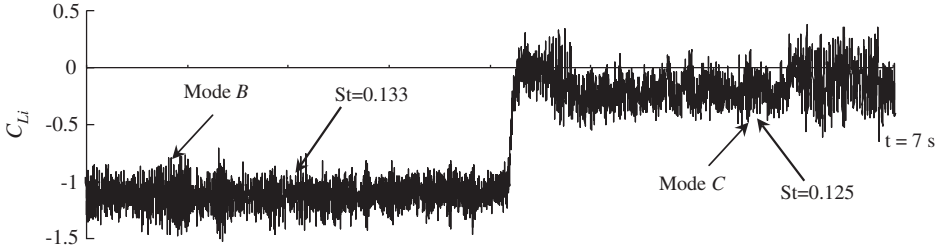

Fig. 16. Lift force signal of upstream cylinder for $T/D = 0.35$, $\alpha = 25^\circ$, indicating a bistable nature of flow.

separation positions of the shear layers (Alam et al., 2003c). The pressure distributions strictly support the separation positions obtained by surface oil-flow patterns, as the separation of flow generally occurs in the pressure recovery region. The major difference in the flow pattern between $T/D = 0.30$ and 0.50 is the existence of a separation bubble for $T/D = 0.30$. That is, if the separation bubble, which forms for $T/D = 0.30$, bursts, the flow pattern for $T/D = 0.30$ will be modified to that for $T/D = 0.50$. Therefore, three different modes of the flow pattern, whose characteristics are definitely different from one another, are established at $T/D = 0.10$, 0.30, and 0.50, respectively.

For simplicity, the flow patterns at $T/D = 0.10$, 0.30, and 0.50, that represent three different modes, can be referred to here as modes A, B and C, respectively. The transition from modes A to B was not found to be discontinuous; but, that from B to C was not only discontinuous but also spontaneous switching from one to the other. The spontaneous switching from modes B to C occurs at $T/D = 0.32$–0.45 (bistable flow region I), which is illustrated by the discontinuous jump in a typical instantaneous lift force signal at $T/D = 0.35$ (Fig. 16). It may be inferred that the bistable flow at $T/D = 0.32$–0.45 is linked to the formation and burst of the separation bubble. Such a kind of the formation and burst of the separation bubble, the bistable nature of the flow, resembles in a way the laminar-separation/ turbulent-reattachment bubble formed on one side of an isolated cylinder at a critical Reynolds number (Bearman, 1969; Kamiya et al., 1979; Farrel and Blessmann, 1983; Schewe, 1983; Almosnino and McAlister, 1984). It is noteworthy that modes A, B and C, at $T/D = 0.10$, 0.30 and 0.50, respectively, are mainly characterized by the behavior of the gap flow between the cylinders. At these spacings, only the outer shear layers predominantly shed vortices, and the two cylinders behave like a single bluff body at least in terms of wake characteristic and Strouhal numbers (Alam and Sakamoto, 2005). It can be mentioned that the Strouhal numbers for modes A, B and C were estimated to be 0.123, 0.133 and 0.125, respectively [see Alam and Sakamoto (2005), for details], suggesting that the effect of the presence or absence of the separation bubble on the vortex shedding frequencies of the outer shear layers is very small.

It can also be observed in Fig. 14 that although C_D and C_L of the upstream cylinder change so briskly in the ranges of $T/D = 0.1$–0.3 and 0.3–0.5, those of the downstream cylinder do not change so in those regions. In other words, though the flow structures around the upstream cylinder are very different between $T/D = 0.10$, 0.30 and 0.50, the flow behind the downstream cylinder is almost the same for the three T/D values. This is corroborated by the surface oil-flow patterns (Fig. 15), which show essentially the same patterns on the downstream cylinder for $T/D = 0.10$, 0.30 and 0.50.

(ii) The region of $1.9 < T/D < 2.1$ is another bistable flow region. The features of the two flow patterns at this bistable flow region are certainly different from those at the bistable flow region I ($T/D = 0.32$–0.45). The second bistable flow region, $1.9 < T/D < 2.1$, is identified as bistable flow region II. It is interesting that the flow over the cylinders in the bistable flow region II at $\alpha = 25^\circ$ is also quite different from that in bistable flow region II at $\alpha = 10^\circ$. At $\alpha = 10^\circ$, in bistable flow region II ($T/D = 2.1$–2.4), the feature of the first flow pattern is that the inner shear layer of the upstream cylinder reattaches onto the downstream cylinder, no alternate vortex shedding occurring behind the upstream cylinder (Fig. 12). On the contrary, at $\alpha = 25^\circ$, in bistable flow region II, the first flow pattern is that the downstream cylinder confronts a mean approaching flow, i.e., the downstream cylinder is outside of the inner shear layer separating the upstream cylinder. The downstream cylinder squeezes the inner shear layer of the upstream cylinder together with a share of mean flow, forming a weak and narrow wake behind the upstream cylinder, as shown in Fig. 17(a). As a result, the frequency of vortex shedding from the upstream cylinder was higher than that from the downstream cylinder or a single cylinder (Alam and Sakamoto, 2005) and the far wake of the upstream cylinder merges with that of the downstream cylinder. In the second flow pattern, Fig. 17(b), the upstream cylinder forms fully developed Karman vortices in synchronization with the downstream cylinder. In other words, the first flow pattern is one which appears for $T/D < 1.9$ and the second flow pattern is one which

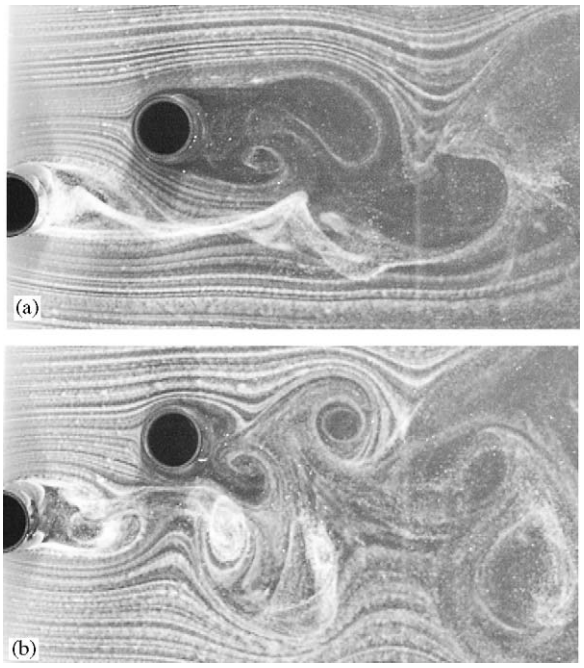

Fig. 17. Visualized flow patterns at $\alpha = 25^{\circ}$: (a) $T/D = 1.9$, (b) $T/D = 2.1$.

appears for $T/D > 2.1$. The second flow pattern induces a greater C_D on the upstream cylinder than the first flow pattern, as fully developed Karman vortices are shed from the upstream cylinder. However, C_L on the upstream cylinder is the same for the two flow patterns (Fig. 14).

(iii) The third noteworthy feature in Fig. 14 is that the downstream cylinder experiences a constant negative lift force at $T/D = 0.5$–1.9, and a higher magnitude of negative lift force at $T/D = 2.1$–4.0, though the approaching flow on the downstream cylinder is almost the free-stream one for both regions of T/D. The flow patterns over the cylinders for the two ranges of T/D are completely different as shown in Fig. 17. The later range of spacing, $T/D = 2.1$–4.0, falls into the so-called '*outer negative lift force*' region in the C_L contours in the T/D versus α plane (Zdravkovich, 1977). As proposed by Mair and Maull (1971), the negative lift force was due to the entrainment of flow into the wake of the upstream cylinder. Using different diameters of the cylinders, i.e., with upstream cylinder larger or lower than the downstream cylinder, lift force measurements by Price (1976) showed that the lift of the downstream cylinder is negligibly affected by the wake characteristics of the upstream cylinder; rather it depends on how much the wake of the upstream cylinder is displaced by the downstream cylinder. In order to acquire insight into the flow pattern which is responsible for the negative lift force, the time-averaged pressure on the surface of the downstream cylinder was measured for $T/D = 1.40$, 1.80 and 2.60, and the results together with flow visualization patterns are shown in Fig. 18. $T/D = 1.40$ (and 1.80) and 2.60 are considered to be representative of the ranges of $T/D = 0.5$–1.9 and 2.1–4.0, respectively. At $T/D = 1.4$ and 1.80 (Fig. 18(a)), it is clear that the stagnation point shifts toward the outer side and it was found to be at $\theta = 10^{\circ}$ and 9° for $T/D = 1.40$ and 1.80, respectively, as estimated from the surface oil-flow patterns. It is also seen that each of the two pressure distributions is almost symmetric about its stagnation points and is almost the same on the inner and outer side surfaces, especially beyond the separation of the shear layers. So, it can be concluded that the negative lift force acting the downstream cylinder at $T/D = 0.5$–1.9 is mainly due to a shift in the stagnation point towards the outer side. It should be mentioned that the position of the stagnation point on the downstream cylinder does not change so much with change in T/D in the range of $T/D = 0.5$–1.9. The stagnation point on the downstream cylinder was found to be at $\theta = 12^{\circ}$, 12°, 10°, and 9° for $T/D = 0.5$, 0.8, 1.4, and 1.8, respectively. However, at $T/D = 2.6$, three factors contribute to the negative lift force: (i) a shift in the stagnation point towards the outer side, the stagnation point occurring at $\theta = 8^{\circ}$ based on the surface oil-flow pattern, (ii) smaller magnitude of pressure on the outer surface, compared with that on an isolated cylinder, and (iii) larger magnitude of pressure on the inner surface. Their contributions to the negative lift force are about 37% ($\theta = -70^{\circ}$ to 70°), 38% ($\theta = 70$–180°) and 25% ($\theta = -70^{\circ}$ to -180°), respectively. It is,

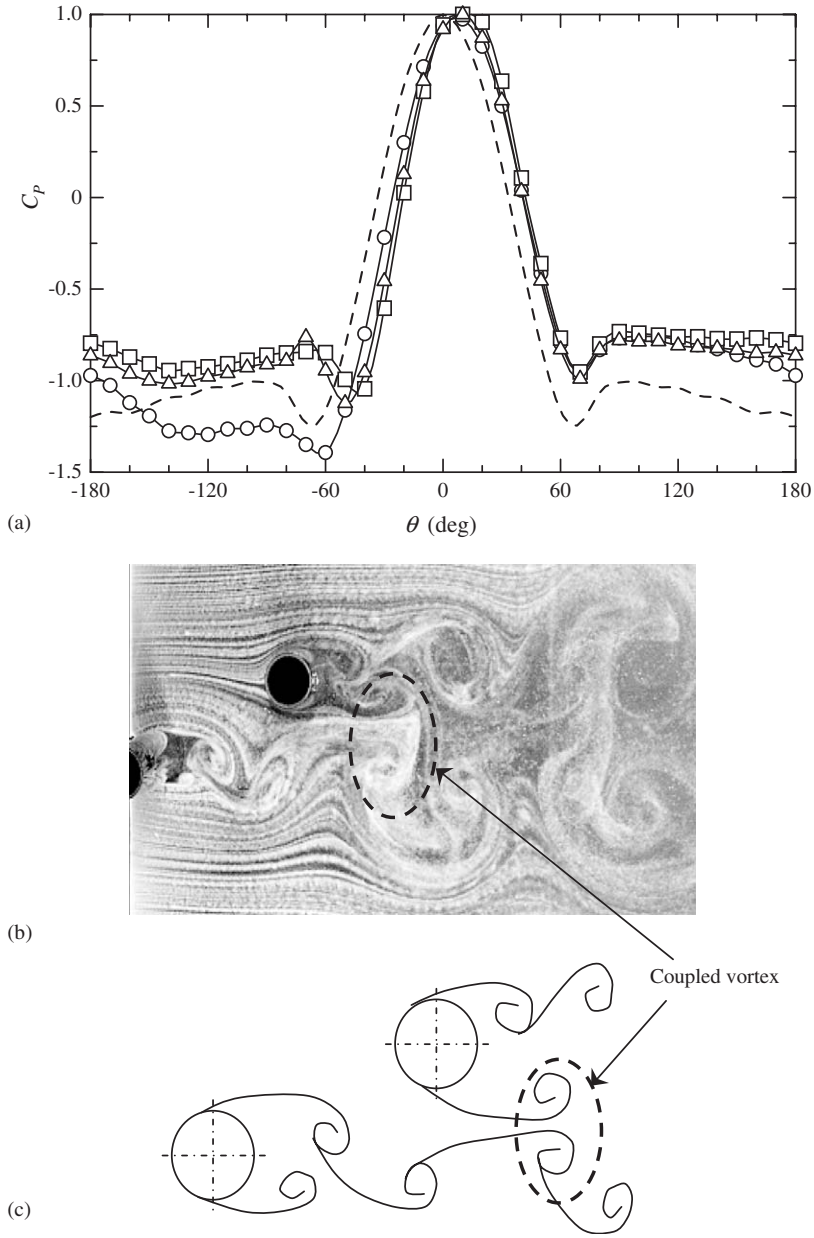

Fig. 18. (a) Time-averaged pressure coefficient distributions on the surface of the downstream cylinder at $\alpha = 25°$: □, $T/D = 1.40$; △, $T/D = 1.80$; ○, $T/D = 2.6$; - - - -, single cylinder. (b) Visualized flow patterns at $\alpha = 25°$, $T/D = 2.6$. (c) Sketch of the flow pattern based on (b).

therefore, clear that the contribution from factor (ii) is the greatest, but it was not pointed out previously. It is an interesting point to ask why the magnitude of pressure on the outside surface for $T/D = 1.4$, 1.8 or 2.6 is lower than that of a single cylinder, though the approaching flow on the downstream cylinder is the free-stream and the near-wake flow of the downstream cylinder is similar to that of a single cylinder. The most probable cause of the lower pressure magnitude on the outside surface is that, with the stagnation point at the outside ($\theta = 10°$ for $T/D = 1.4$, $\theta = 9°$ for $T/D = 1.8$ and $\theta = 8°$ for $T/D = 2.6$), the effective flow width on the outer surface of the bluff body becomes smaller than that when the stagnation point occurs at $\theta = 0°$; that is, the flow blows over the outside surface of the downstream cylinder having a smaller effective bluffness than a single cylinder, resulting in a lower

pressure magnitude on the base surface as well as on the outer side surface. On the other hand, the larger magnitude of negative pressure on the inside surface at $T/D = 2.6$ is partly contributed from the highly negative pressure on the wake center-line of the upstream cylinder, and the highly negative pressure on the wake center-line also increases the flow rate through the gap between the cylinders since the fully developed Karman vortices are formed behind the upstream cylinder for $T/D > 2.1$. Furthermore, it cannot be ignored that inner vortices shed from the downstream cylinder are coupled with those from the upstream cylinder, thus increasing the velocity of flow on the inner surface of the downstream cylinder. It can be noted that for $T/D > 2.1$ the frequency of vortex shedding from the downstream cylinder is synchronized with that from the upstream cylinder, and the inner vortices of downstream cylinder are coupled with the incoming vortices from the inner surface of the upstream cylinder (Alam and Sakamoto, 2005), as shown in Figs. 18(b, c). It is known that, when two opposite sign vortices are coupled, their velocity increases significantly (Couder and Basdevant, 1986). Hence, a higher velocity of flow on the inside surface of the downstream cylinder can be expected from a contribution of the vortex coupling, resulting in a higher negative pressure on the inside surface of the downstream cylinder.

Fig. 19 shows C_D' and C_L' distributions of both cylinders at $\alpha = 25^\circ$. Here also, a sudden change in C_D' and C_L' in the ranges of $T/D = 0.10$–0.30 and 0.30–0.50 occurs due to the change of mode from A to B and B to C, respectively. Mode B, in which a separation bubble forms on the inside surface of the upstream cylinder, induces a minimum C_L' on the upstream and downstream cylinders. That is, the near wake of the cylinders in mode B is more tranquil than that in modes A or C. At $T/D = 0.6$–1.9, the values of C_D' and C_L' of the upstream cylinder are very small, indicating a relatively steady near-wake of the upstream cylinder. C_D' and C_L' experience a large discontinuous jump in the bistable flow region $T/D = 1.9$–2.1, where the fully developed Karman vortices behind the upstream cylinder begin to appear intermittently. It is seen that the values of C_D' and C_L' of the downstream cylinder are greater than those of the upstream cylinder for the range of spacing examined, as found for tandem arrangement (Alam et al., 2003c) and for $\alpha = 10^\circ$ (Section 3.2).

A striking feature in Fig. 19 is that, as T/D reaches 5.0, C_D' and C_L' of the upstream cylinder approach the single cylinder values, but those of the downstream cylinder are considerably larger for $T/D > 2.1$. Furthermore, C_D' of the downstream cylinder decreases with increase in T/D for $T/D > 2.1$, though C_L' of the downstream cylinder retains its higher value ($C_L' \approx 0.78$) even up to $T/D = 5.0$, indicating at least one characteristic of the flow on the downstream cylinder does not change with changing T/D. In order to acquire information about the characteristics of the flow around the upstream cylinder at $T/D = 0.6$–1.9 (at which the values of C_D' and C_L' of upstream cylinder are very low) and about the characteristics of the flow on the downstream cylinder for $T/D > 2.1$ (at which the values of C_D' and C_L' of the downstream cylinder are very high), fluctuating pressures on the surfaces of the cylinders were measured for $T/D = 1.40$, 2.60 and 5.0 and the results, together with flow visualization patterns in this range, are shown in Fig. 20. Fluctuation of pressure on the entire surface of the upstream cylinder at $T/D = 1.40$ is very low, that corroborates that at least the near-wake flow of the upstream cylinder is tremendously steady, as seen in the flow visualization pattern (Fig. 20(b)). Such a low fluctuation of pressure on the entire surface of the upstream cylinder, an almost uniform fluctuating pressure distribution, was also observed in the case of two tandem cylinders (Igarashi, 1981; Alam et al., 2003c) and at $\alpha = 10^\circ$ ($T/D = 1.3$–2.1). The fluctuating pressure distribution on the downstream cylinder at $T/D = 2.60$ shows that the value of C_P' on the inside surface is extremely high. The extremely high fluctuation of pressure on the inside surface is due to the interaction of strong rolling incident vortices from the upstream cylinder with the inside surface of the downstream cylinder (Gursul and Rockwell, 1990; Tang and Rockwell, 1983; Lee and Smith, 1991; Rockwell, 1998). The flow pattern at $T/D = 2.6$ has already been shown in Fig. 18(b). Fluctuating pressure on the surface of the downstream cylinder is supposed to be a strong function of the transverse offset of the downstream cylinder with respect to the incident vortices from the upstream cylinder and the degree of vorticity of the incident vortices, as investigated by Ziada and Rockwell (1982), Rockwell (1983), Tang and Rockwell (1983), Gursul and Rockwell (1990) and Park and Lee (1994). They found in their experiment that the fluctuation of pressure attains its maximum value approximately at the location on the surface near where the vortices roll up or where the trajectory of the vortex street is closest. So, at and near $T/D = 2.6$, the fluctuating drag and lift forces of the downstream cylinder are strong mainly due to the higher fluctuation of pressure on the inside surface, and the higher fluctuation of pressure on the inside surface is due to the alternating buffeting of the incident vortices during convection on the inside surface of the downstream cylinder. A comparison of C_P' distributions at $T/D = 2.6$ and 5.0 reveals that, as T/D increases from 2.6 to 5.0, the value of C_P' decreases and increases, respectively, on the inside and outside surfaces of the downstream cylinder; that is, the direct interaction of the incident vortices tending to increase the fluctuating pressure on the inside surface of the downstream cylinder decreases as T/D increases. Since, even at $T/D = 5.0$, the value of C_P' on either side is substantially strong in comparison with that of a single cylinder, it can be assumed that the flow over the downstream

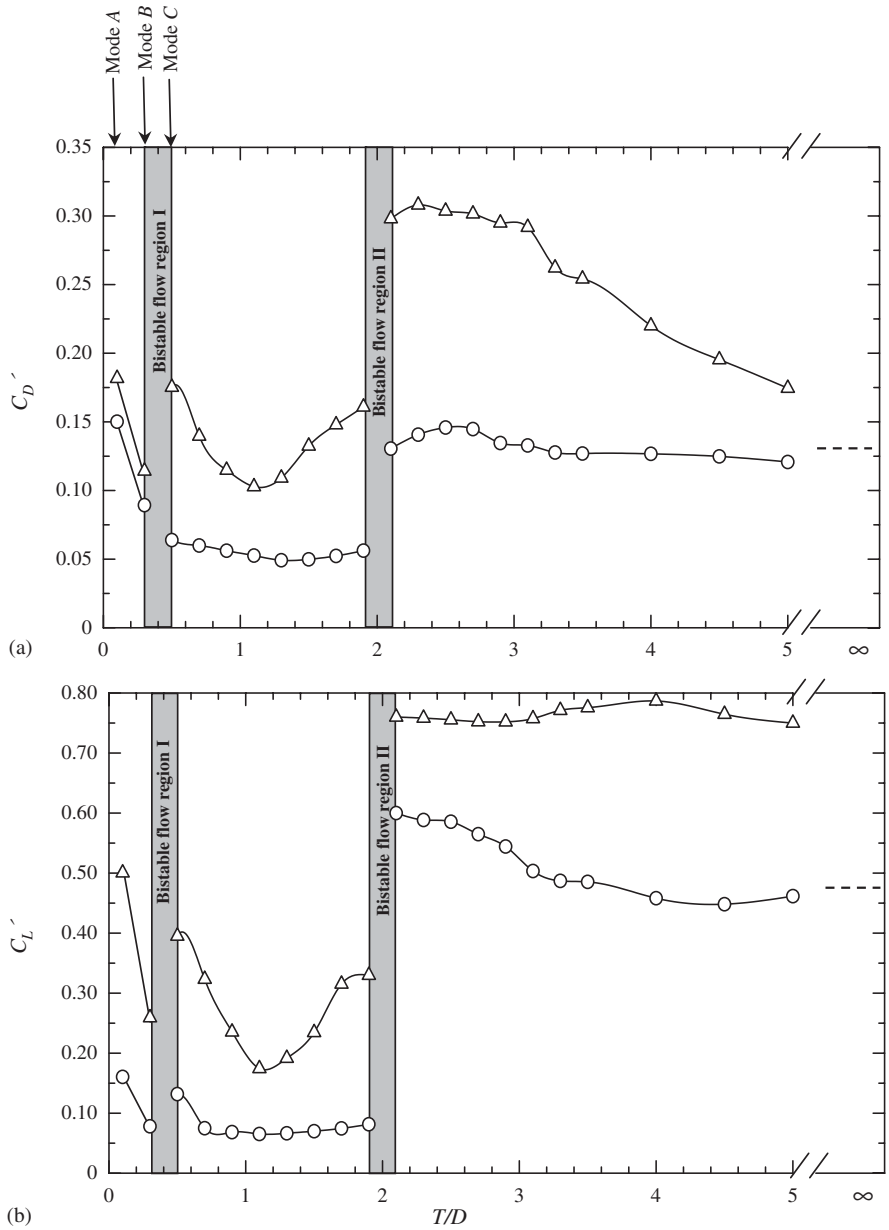

Fig. 19. Fluctuating drag and lift coefficient distributions at $\alpha = 25^{\circ}$: (a) C_P', (b) C_L'; ○, upstream cylinder; △, downstream cylinder; ---, single cylinder.

cylinder is fairly enhanced, which induces the higher C_L' (Fig. 19) and the higher C_D (Fig. 14) on the downstream cylinder. At $T/D = 2.1$–5.0, vortex shedding from the inside of the downstream cylinder was found to be synchronized and coupled with the incident vortices from the inside of the upstream cylinder. The flow visualization patterns in Figs. 20(c, d) corroborate that the far-wake of the upstream cylinder becomes wider and enhanced as vortices move to the downstream, inducing synchronized and enhanced vortex shedding from the downstream cylinder. It is seen in the figures that the inner vortices from the upstream and downstream cylinders form coupled vortices. A coupled vortex looks like a cat's eyes. The synchronization of vortex shedding from the inside of the downstream cylinder with the incident vortices from the upstream cylinder and the formation of coupled vortices are the common characteristics of the flow pattern in the range of $T/D = 2.1$–5.0 examined.

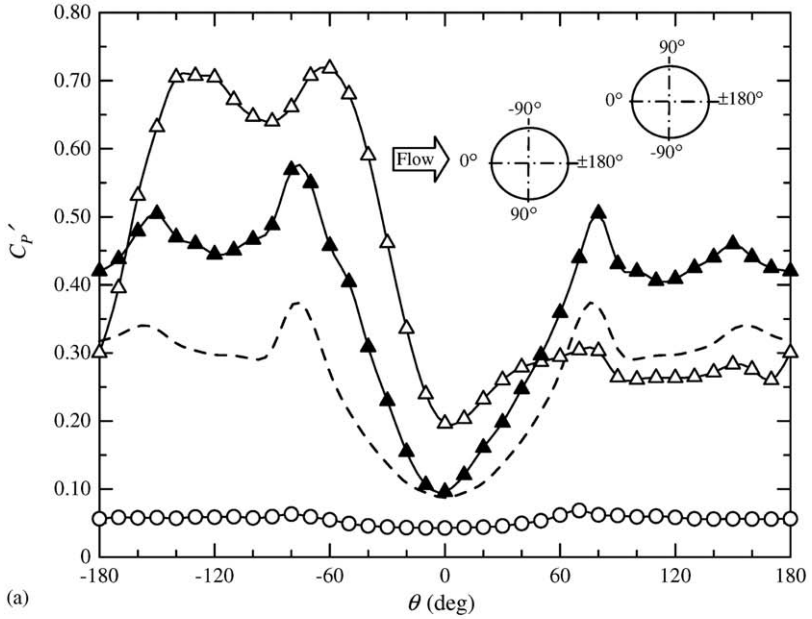
0.80
0.70
0.60
0.50
0.40
0.30
0.20
0.10
0
C_p'
-180
-120
-60
0
60
120
180
θ (deg)
Flow
0°
±180°
-90°
90°
90°
0°
±180°
-90°

(a)

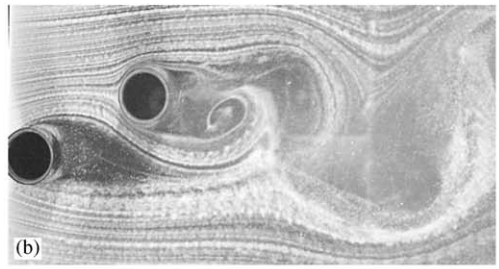
(b)

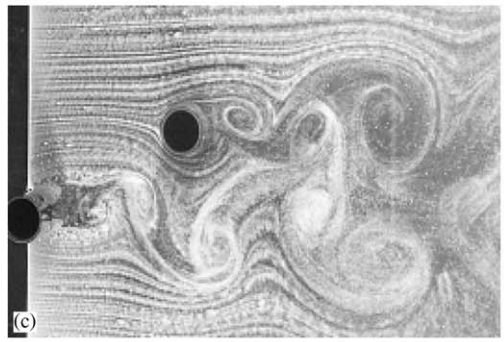
(c)

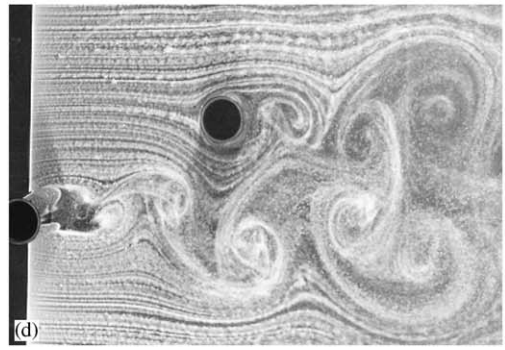
(d)

3.4. Staggered arrangement with $\alpha = 45^\circ$

Fig. 21 shows C_D, C_D', C_L and C_L' distributions of the upstream and downstream cylinders at $\alpha = 45^\circ$. The C_D and C_L distributions at $\alpha = 45^\circ$ are quite different from those at $\alpha = 25^\circ$ (Fig. 14). C_D, C_L, C_D' and C_L' of both cylinders are seen to approach those of a single cylinder when T/D reaches 5.0. The bistable nature of the flow, which was due to the intermittent appearance and disappearance of a fully developed Karman vortex behind the upstream cylinder at $\alpha = 25^\circ$, was not found at $\alpha = 45^\circ$. In this case, the narrower wake of the upstream cylinder gradually reaches a fully developed Karman wake (single cylinder wake). At very small spacing, in the range of $T/D = 0.10$–0.30, a sudden drop in C_D, C_L, C_D' and C_L' of each cylinder is seen in the figure. As a bistable flow was found at $0.30 < T/D < 0.50$ at $\alpha = 25^\circ$ (Section 3.3), where a sudden change in C_L of the upstream cylinder occurred due to the formation and burst of a separation bubble, that kind of bistable flow is also expected in the range of $T/D = 0.10$–0.30 at $\alpha = 45^\circ$. For $\alpha = 25^\circ$, the lift force acting on the upstream cylinder was highly negative at $T/D = 0.30$. Now at $\alpha = 45^\circ$, there is no sign of the negative lift force of the upstream cylinder, rather there is a higher magnitude of positive lift at $T/D = 0.10$.

In order to elucidate the flow pattern that corresponds to the positive lift force acting on the upstream cylinder at $T/D = 0.10$ and the change in the flow pattern between $T/D = 0.10$ and 0.30, time-averaged pressure distributions, surface oil-flow patterns and corresponding sketches of the flow pattern at $T/D = 0.10$ and 0.30 are shown in Fig. 22. At $T/D = 0.10$, at which the value of C_L of the upstream cylinder is highly positive and the value of C_D is greatest in magnitude, the pressure distribution implies two reasons for generating such a high magnitude of positive lift force: one is a shift in the stagnation point to the inner side and the other is the development of high pressure, compared with that on a single cylinder, at $\theta = -20^\circ$ to -130° on the inside surface. It is seen that the inner shear layer of the upstream cylinder firstly separates at $\theta = -89^\circ$, i.e., in the first pressure recovery region, and the pressure is still positive near the first separation, suggesting that pressure gradient at $\theta = 0^\circ$ to -70° is substantially smaller than the single cylinder case. This is because the flow on the inside surface of the upstream cylinder is obstructed by the front surface of the downstream cylinder. As the gap width between the cylinders is very small in this case, the inner shear layer of the upstream cylinder is forced to reattach again onto the rear part of the inside surface and separates eventually at $\theta = -141^\circ$, i.e., in the second pressure recovery region. Hence, a separation bubble is formed on the inside surface of the upstream cylinder. It is interesting that a high pressure gradient occurs in the range of $\theta = -100^\circ$ to -135° where the gap flow passage is like a convergent nozzle and pressure on the surface reaches its maximum negative value at $\theta = -(180—45^\circ) = -135^\circ$, where the gap width between the surfaces of the cylinders is minimum. Beyond $\theta = -135^\circ$, the flow passage can be considered to be a divergent nozzle. So the gap flow separates from both the cylinders just after the point where the gap width between the surfaces is the minimum. That is, the gap flow separates from the upstream and downstream cylinders at $\theta = -141^\circ$ and -48°, respectively, just 6° ($= |-141^\circ-(-135^\circ)|$) and 3°($= |-48^\circ-(-45^\circ)|$) farther than the minimum gap width point. At $T/D = 0.30$, the pressure distribution has almost a similar trend on both sides, except for a somewhat lower pressure gradient on the inner side surface than that of the outer side surface or that of the single cylinder. In this case the stagnation line is at -8° and the inner shear layer of the upstream cylinder separates at -127° without forming any separation bubble. In the region of $T/D = 0.10$–0.30, the change in the flow pattern from that at $T/D = 0.10$ to that at $T/D = 0.30$ was found to be discontinuous due to the appearance and disappearance of the separation bubble, as found for $\alpha = 25^\circ$ also. Nevertheless, a spontaneous switch from one flow pattern to the other was not observed.

Fig. 22 shows that there is a significant difference in the flow structures on the upstream cylinder at $T/D = 0.10$ and 0.30; however, the flow structure on the downstream cylinder at those spacings are the same in nature. Hence, it may be concluded that the inner shear layer around the upstream cylinder plays the main role in the significant change in C_L of the upstream cylinder.

For $\alpha \leqslant 25^\circ$, it was found that the values of C_D' and C_L' of the downstream cylinder were always greater than those of the upstream cylinder, and the value of C_D of the downstream cylinder was considerably smaller than that of the upstream cylinder except at $\alpha = 25^\circ$, $T/D > 3.5$. Here, the value of C_D of the downstream cylinder is somewhat greater than that of the upstream cylinder for $T/D > 0.7$, implying the downstream cylinder is completely outside the wake of the upstream cylinder; however, the downstream cylinder forces the flow on the inside surface of the upstream cylinder to form a narrower wake behind the upstream cylinder (Alam and Sakamoto, 2005).

In Fig. 21, it is seen that the values of C_D' and C_L' of the downstream cylinder do not exceed those of a single cylinder; in contrast with case of $\alpha = 25^\circ$, the downstream cylinder experienced higher magnitudes of C_D' and C_L' for

Fig. 20. (a) Fluctuating pressure coefficient distributions $\alpha = 25^\circ$: ○, $T/D = 1.40$, upstream cylinder; △, $T/D = 2.6$, downstream cylinder; ▲, $T/D = 5.0$, downstream cylinder; ----, single cylinder. (b, c, d) Visualized flow patterns $\alpha = 25^\circ$: (b) $T/D = 1.40$; (c) $T/D = 3.0$; (d) $T/D = 4.0$.

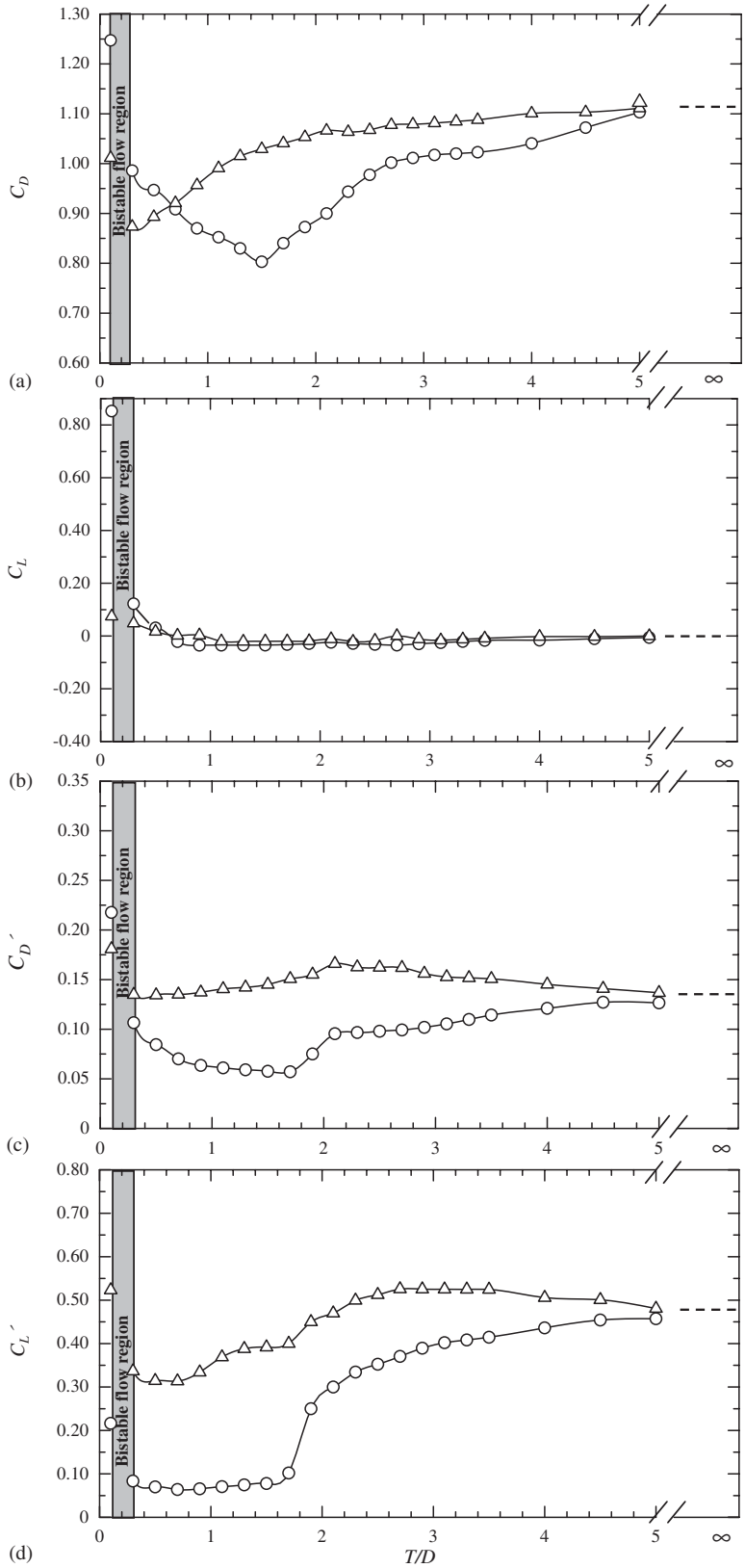

Fig. 21. Fluid force coefficient distributions for $\alpha = 45^{\circ}$: (a) C_D, (b) C_L, (c) C'_D, (d) C'_L; ○, upstream cylinder; △, downstream cylinder; ---, single cylinder.

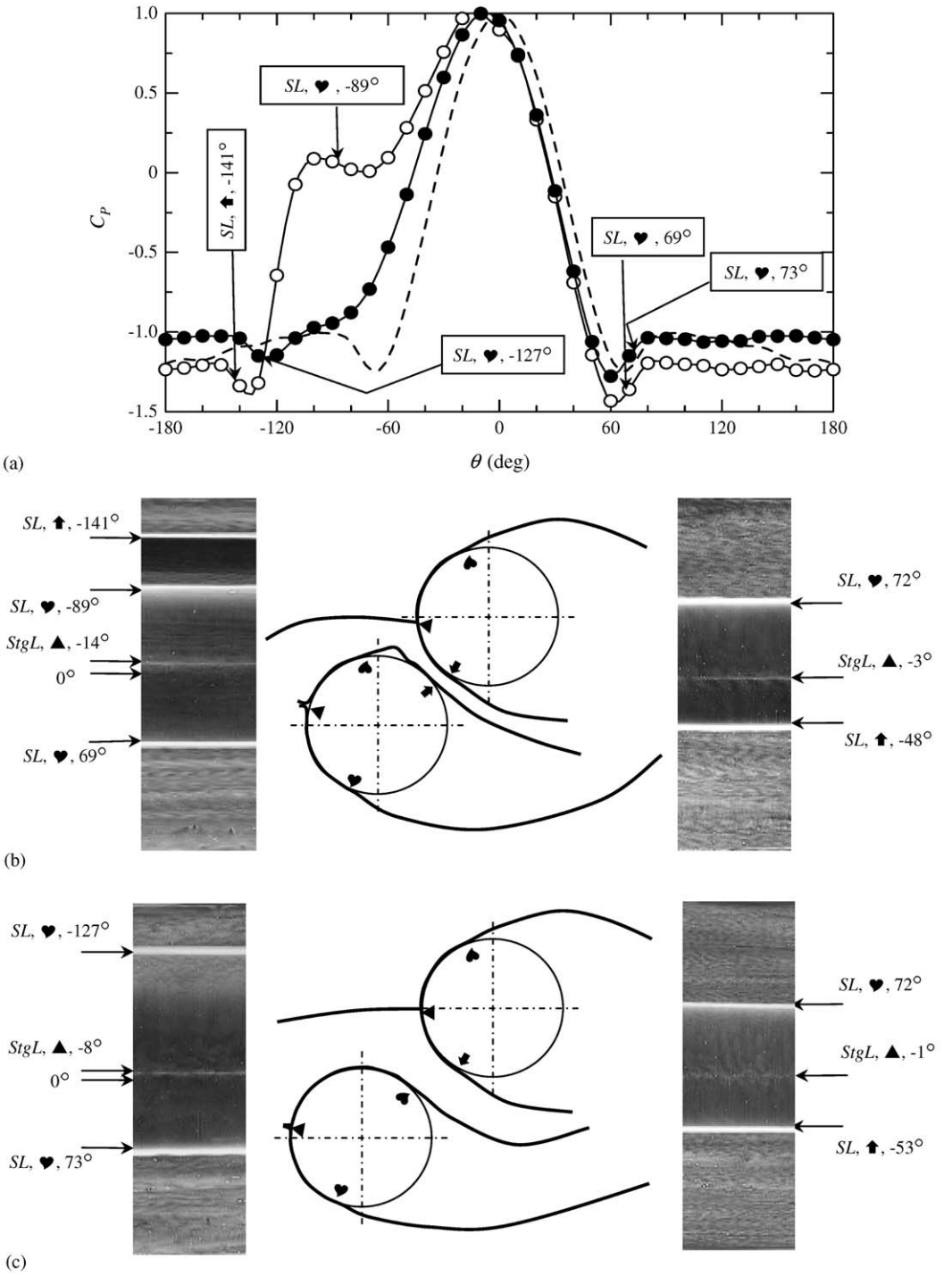

Fig. 22. (a) Time-averaged pressure coefficient distribution of upstream cylinder for $\alpha = 45^{\circ}$: ○, $T/D = 0.10$; ●, $T/D = 0.30$; ----, single cylinder; (b) surface oil-flow patterns and sketch of flow $T/D = 0.10$; (c) surface oil-flow patterns and sketch of flow $T/D = 0.30$.

$T/D > 2.0$ due to synchronized and coupled vortex shedding from the downstream cylinder. As enhanced vortex shedding from the downstream cylinder was found to occur for $T/D > 2.0$, $\alpha = 25^{\circ}$, such a kind of enhanced vortex shedding does not occur at $\alpha = 45^{\circ}$. This is due to fact that now, at $\alpha = 45^{\circ}$, the inner-row vortices from the upstream

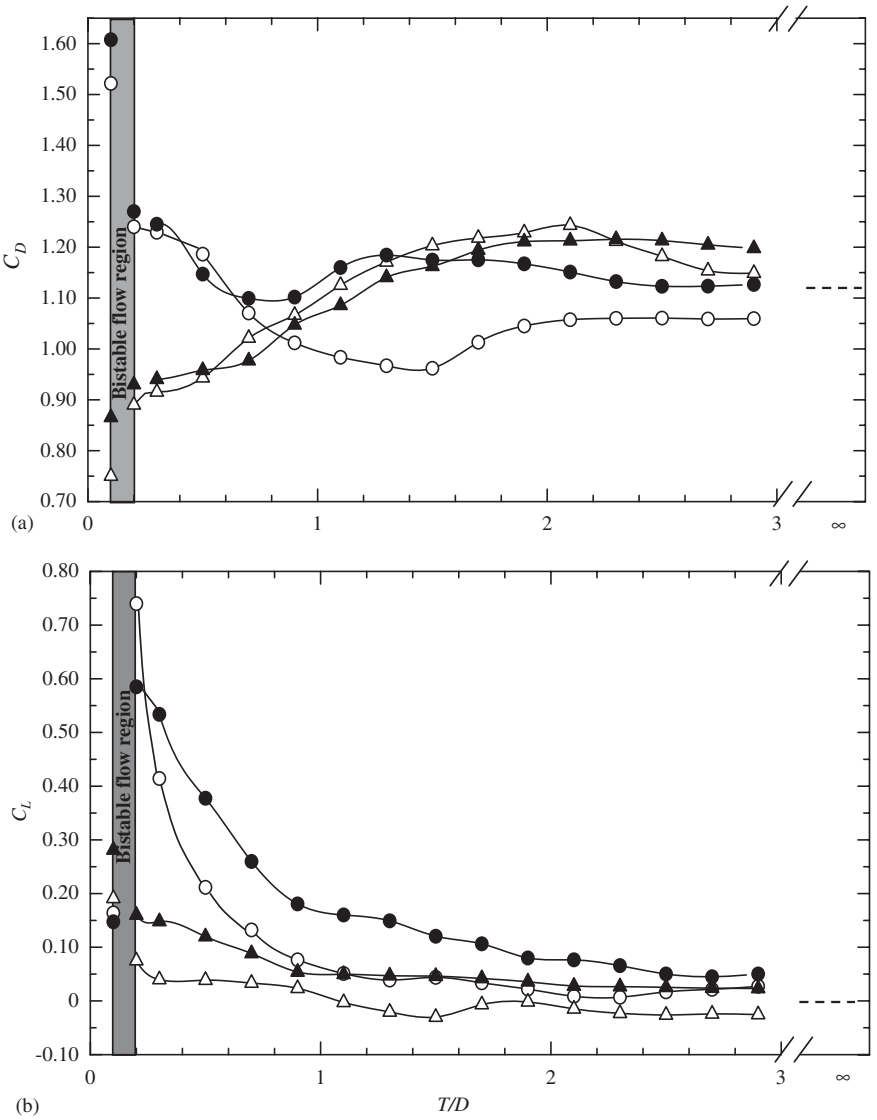

Fig. 23. Time-averaged drag and lift coefficient distributions: (a) C_D, (b) C_L; ○, upstream cylinder, $\alpha = 60^{\circ}$; △, downstream cylinder, $\alpha = 60^{\circ}$; ●, upstream cylinder, $\alpha = 75^{\circ}$; ▲, downstream cylinder, $\alpha = 75^{\circ}$.

cylinder are quite far from the inner surface of the downstream cylinder. Thus the formation of vortices from the inside surface of the downstream cylinder is not triggered by the inner-row vortices from the upstream cylinder, and no enhanced flow on/behind the downstream cylinder is generated. Also, the negative lift force ('outer lift peak'), which was found at $\alpha = 25^{\circ}$, is completely absent at $\alpha = 45^{\circ}$.

3.5. *Staggered arrangement with $\alpha = 60^{\circ}$ and 75°*

Fig. 23 shows the dependence on T/D of C_D and C_L of both cylinders at $\alpha = 60^{\circ}$ and 75°. The measurements were conducted up to $T/D = 5.0$, but the data of $T/D < 3.0$ only are shown to highlight the C_D and C_L variations at small T/D. Note that the values of C_D, C_L, C_D' and C_L' of each cylinder approached those of a single cylinder at $T/D = 4.0$. It is seen that the trends of C_D and C_L distributions at $\alpha = 60^{\circ}$ are almost identical with those at $\alpha = 75^{\circ}$. For $T/D < 0.7$, where both cylinders behave like a single bluff body in terms of the Strouhal number (Alam and Sakamoto, 2005), the value of C_D of the upstream cylinder is greater than that of the downstream cylinder. The gap flow is highly biased

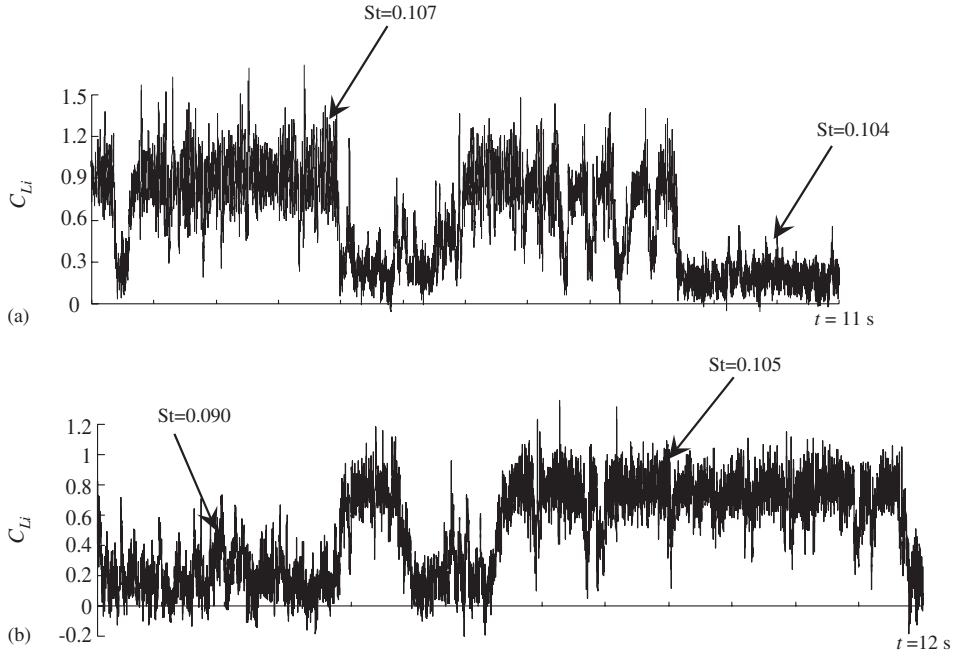

Fig. 24. Lift force signal of upstream cylinder, indicating a bistable nature of flow: (a) $T/D = 0.12$, $\alpha = 60^{\circ}$, (b) $T/D = 0.13$, $\alpha = 75^{\circ}$.

toward the wake center-line of the upstream cylinder for $T/D < 0.7$, resulting in higher drag on the upstream cylinder. An interesting feature of the C_D and C_L distributions is that, as T/D increases from 0.10 to 0.20, C_D of the upstream cylinder suddenly drops from a higher value to a lower one, and C_L suddenly jumps from a lower value to a higher one; then C_D and C_L change gradually for $T/D > 0.20$. In the range of $0.10 < T/D < 0.20$, a bistable flow was detected and the fluid force coefficients for the two flow patterns were as those at $T/D = 0.10$ or 0.20; that is, the range $0.10 < T/D < 0.20$ is a bistable flow region, at which two flow patterns appear alternately. Hence, the first flow pattern is expected to be the one which appears at $T/D = 0.10$ and the second flow pattern is one which appears at $T/D = 0.20$. Typical lift force signals showing the bistable nature of the flow are presented in Fig. 24. C_L distribution of the upstream cylinder at $\alpha = 60^{\circ}$ and 75° is similar to that at side-by-side circular cylinders (Alam et al., 2003a). Results of C_L measurements for side-by-side arrangement by Alam et al. (2003a) also showed a large variation in C_L of the cylinder associated with the narrow wake between $T/D = 0.1$ and 0.2.

Here, time-averaged pressure measurements and surface oil-flow patterns evidenced that the main difference between the two flow patterns of the upstream cylinder at $T/D = 0.10$ and 0.20 is the presence of a separation bubble on the side surface and an occurrence of a turbulent reattachment in the base region at $T/D = 0.10$, and the absence of the separation bubble as well as the turbulent reattachment at $T/D = 0.20$. That is, mainly the occurrence of the turbulent reattachment and detachment in the base region of the upstream cylinder regulates the bistable flow. It is seen in the signals that, though there is a large difference in C_L magnitude between the two modes, the difference in Strouhal number is very small, indicating that the presence or absence of the separation bubble on the inside surface of the upstream cylinder has great influence on the magnitude of C_L, but has a little influence on the Strouhal number.

4. Conclusions

Fluid forces and flow characteristics of two identical circular cylinders in staggered configurations at $\alpha = 10^{\circ}$, 25°, 45°, 60°, and 75° in the range of $T/D = 0.1$–5.0 were investigated at a Reynolds number of 5.5×10^4. The main results are summarized as follows:

(i) Four kinds of bistable flow on two circular cylinders in staggered arrangements are found in this study. The four kinds of bistable flow appear in different regions and have distinct characteristics. The first kind of bistable flow is

due to intermittent reattachment and detachment of only the inner shear layer of the upstream cylinder onto the downstream cylinder and it occurs at $\alpha = 10^\circ$, $T/D = 2.1$–2.4. The second kind of bistable flow is due to the intermittent formation of a narrower wake and a fully developed Karman wake behind the upstream cylinder and is observed at $\alpha = 25^\circ$, $T/D = 1.9$–2.1. The third kind of bistable flow is linked to the formation and burst of a separation bubble, which is formed on the inside surface of the downstream cylinder. It appears at $\alpha = 10^\circ$, $T/D = 0.1$–1.3. The fourth kind of bistable flow is ascribed to the formation and burst of a separation bubble on the inside surface of the upstream cylinder or to turbulent reattachment and detachment of the inner shear layer on the rear surface of the upstream cylinder. It usually occurs at very close spacings: $\alpha = 25^\circ$, $T/D = 0.3$–0.5; $\alpha = 45^\circ$, $T/D = 0.1$–0.3; $\alpha = 60^\circ$, $T/D = 0.1$–0.2; and $\alpha = 75^\circ$, $T/D = 0.1$–0.2. The bistable flow caused by the formation and burst of a separation bubble on a cylinder (the third and fourth kinds) gives rise to a greater difference in the lift force on that cylinder only; on the other hand, the bistable flow caused by the intermittent reattachment and detachment of a shear layer from the upstream cylinder onto the downstream cylinder (the first kind) produces a greater difference in time-averaged drag, fluctuating drag and fluctuating lift on both cylinders between the two stable states. The second kind bistable flow causes a greater difference in fluctuating drag and fluctuating lift on both cylinders between the two stable states.

(ii) The lift force is highly negative on the downstream cylinder at $\alpha = 10^\circ$, $T/D = 0.9$ and on the upstream cylinder at $\alpha = 25^\circ$, $T/D = 0.3$. The highly negative lift force acting on the upstream cylinder at $\alpha = 25^\circ$, $T/D = 0.3$ is largely attributed to a large circulation associated with the gap flow on the inside and rear surfaces of the upstream cylinder. The upstream cylinder experiences a highly positive lift force at $\alpha = 45^\circ$, $T/D = 0.1$; $\alpha = 60^\circ$, $T/D = 0.2$; and $\alpha = 75^\circ$, $T/D = 0.2$. The highly positive lift force is due to a shift in the stagnation point towards the inside surface of the upstream cylinder and the retardation of the flow on the inside surface of the upstream cylinder by the front surface of the downstream cylinder.

(iii) The maximum fluctuating drag force on the downstream cylinder occurs at $\alpha = 10^\circ$, $T/D = 2.4$–3.0, where the inner shear layer of the upstream cylinder rolls just ahead of the front surface of the downstream cylinder.

(iv) The maximum fluctuating lift force on the downstream cylinder is 0.78 at $\alpha = 25^\circ$, $T/D = 2.1$–5, resulting from the synchronization of vortex shedding from the inner side of the downstream cylinder with incident inner vortices from the upstream cylinder. An interaction of the incident vortices from the upstream cylinder with the downstream cylinder and an occurrence of synchronized vortex shedding cause such a high fluctuating lift force on the downstream cylinder.

(v) The change from the presence to absence (or *vice versa*) of a separation bubble or turbulent shear layer reattachment is always associated with a discontinuous change in the flow structure and both flow states are stable.

References

Abdulhadi, M., 1985. Aerodynamic forces on bluff structures on a wake. Journal of Wind Engineering and Industrial Aerodynamics 21, 101–115.

Akosile, O.O., Sumner, D., 2003. Staggered circular cylinders immersed in a uniform planner shear flow. Journal of Fluids and Structures 18, 613–633.

Alam, M.M., 2004. Aerodynamic characteristics and suppression of fluid forces acting on two bluff bodies in various arrangements and multistable flow detection by wavelets. Ph.D. Thesis, Kitami Institute of Technology, Japan.

Alam, M.M., Sakamoto, H., 2005. Investigation of Strouhal frequencies of two staggered bluff bodies and detection of multistable flow by wavelets. Journal of Fluids and Structures 20, 425–449.

Alam, M.M., Moriya, M., Takai, K., Sakamoto, H., 2002. Suppression of fluid forces acting on two square cylinders in a tandem arrangement by passive control of flow. Journal of Fluids and Structures 16, 1073–1092.

Alam, M.M., Moriya, M., Sakamoto, H., 2003a. Aerodynamic characteristics of two side-by-side circular cylinders and application of wavelet analysis on the switching phenomenon. Journal of Fluids and Structures 18, 325–346.

Alam, M.M., Sakamoto, H., Moriya, M., 2003b. Reduction of fluid forces acting on a single circular cylinder and two circular cylinders by using tripping rods. Journal of Fluids and Structures 18, 347–366.

Alam, M.M., Moriya, M., Takai, K., Sakamoto, H., 2003c. Fluctuating fluid forces acting on two circular cylinders in a tandem arrangement at a subcritical Reynolds number. Journal of Wind Engineering and Industrial Aerodynamics 91, 139–154.

Almosnino, D., McAlister, K.W., 1984. Water tunnel study of transition flow around circular cylinders. National Aeronautics and Space Administration, NASA Report 85879.

Batham, J.P., 1973. Pressure distribution on circular cylinders at critical Reynolds numbers. Journal of Fluid Mechanics 57, 209–228.

Bearman, P.W., 1969. On vortex shedding from a circular cylinder in the critical Reynolds number regime. Journal of Fluid Mechanics 37, 577–585.

Bokaian, A., Geoola, F., 1984. Wake-induced galloping of two interfering circular cylinders. Journal of Fluid Mechanics 146, 383–415.

Chen, S.S., 1986. A review of flow-induced vibration of two circular cylinders in crossflow. ASME Journal of Pressure Vessel Technology 108, 382–393.

Cooper, K.R., 1973. Wind tunnel and theoretical investigations into the aerodynamic instability of smooth and stranded twin bundles power conductors. National Aeronautical Establishment Report LTR-LA-115, Ottawa, Canada.

Couder, Y., Basdevant, C.B., 1986. Experimental and numerical study of vortex couples in two-dimensional flows. Journal of Fluid Mechanics 173, 225–251.

Farrel, C., Blessmann, J., 1983. On critical flow around smooth circular cylinders. Journal of Fluid Mechanics 136, 375–391.

Gu, Z., Sun, T., 1999. On interference between two circular cylinders in staggered arrangement at high subcritical Reynolds numbers. Journal of Wind Engineering and Industrial Aerodynamics 80, 287–309.

Gu, Z.F., Sun, T.F., He, D.X., Zhang, L.L., 1993. Two circular cylinders in high-turbulence flow at supercritical Reynolds number. Journal of Wind Engineering and Industrial Aerodynamics 49, 379–388.

Gursul, I., Rockwell, D., 1990. Vortex street impinging upon an elliptical leading edge. Journal of Fluid Mechanics 211, 211–242.

Hori, E., 1959. Experiments on flow around a pair of parallel circular cylinders. Proceeding of 9th Japan National Congress for Applied Mechanics, Paper III-11, pp. 231–234.

Igarashi, T., 1981. Characteristics of the flow around two circular cylinders arranged in tandem, (1st Report). Bulletin of the Japan Society of Mechanical Engineers 24, 323–331.

Igarashi, T., 1984. Characteristics of the flow around two circular cylinders arranged in tandem (2nd Report). Bulletin of the Japan Society of Mechanical Engineers 27, 2380–2387.

Ishigai, S., Nishikawa, E., Nishimura, E., Cho, K., 1972. Experimental study of structure of gas flow in tube banks axes normal to flow. Bulletin of the Japan Society of Mechanical Engineers 15, 949–956.

Kamiya, N., Suzuki, S., Nishi, T., 1979. On the aerodynamic force acting on a circular cylinder in the critical range of the Reynolds number. AIAA Meeting, Paper 79-1975.

Keser, H.I., Unal, M.F., 2003. Flow around a circular cylinder downstream of blunt-based flat plate in tandem and staggered arrangements. Journal of Fluids and Structures 17, 783–791.

Kiya, M., Arie, M., Tamura, H., Mori, H., 1980. Vortex shedding from two circular cylinders in staggered arrangement. ASME Journal of Fluids Engineering 102, 166–173.

Ko, N.W.M., Wong, P.T.Y., 1992. Flow past two circular cylinders of different diameters. Journal of Wind Engineering and Industrial Aerodynamics 41–44, 563–564.

Lee, D.J., Smith, C.A., 1991. Effect of vortex core distortion on blade–vortex interaction. AIAA Journal 29, 1355–1363.

Liu, C.H., Chen, J.M., 2002. Observations of hysteresis in flow around two square cylinders in a tandem arrangement. Journal of Wind Engineering and Industrial Aerodynamics 90, 1019–1050.

Mair, W.A., Maull, D.J., 1971. Aerodynamic behavior of bodies in the wakes of other bodies. Philosophycal Transactions of the Royal Society of London A 269, 425–437.

Medeiros, E.B., Zdravkovich, M.M., 1992. Interference-induced oscillation of two unequal cylinders. Journal of Wind engineering and Industrial Aerodynamics 41–44, 753–762.

Moriya, M., Sakamoto, H., 1985. Fluctuating fluid forces acting on a downstream circular cylinder in the staggered arrangement. Transactions of the Japan Society of Mechanical Engineers 51, 2098–2104 (in Japanese).

Norberg, C., 2003. Fluctuating lift on a circular cylinder: review and new measurements. Journal of Fluids and Structures 17, 57–96.

Park, J.H., Lee, D.J., 1994. Numerical simulation of vortex–wedge interaction. AIAA Journal 32, 1126–1134.

Price, J., 1976. The origin and nature of the lift force on the leeward of two bluff bodies. Aeronautical Quarterly 26, 154–168.

Price, S.J., Paidoussis, M.P., 1984. The aerodynamic forces acting on groups of two and three circular cylinders when subject to a cross-flow. Journal of Wind Engineering and Industrial Aerodynamics 17, 329–347.

Rockwell, D., 1983. Oscillation of impinging shear layers. AIAA Journal 21, 645–661.

Rockwell, D., 1998. Vortex–body interactions. Annual Review of Fluid Mechanics 30, 199–229.

Sakamoto, H., Oiwake, S., 1984. Fluctuating forces on a rectangular prism and a circular cylinder placed vertically in a turbulent boundary layer. ASME Journal of Fluids Engineering 106, 160–166.

Sakamoto, H., Haniu, H., Obata, Y., Matubara, S., 1994. Optimum suppression of fluid forces acting on a circular cylinder and its effectiveness. JSME International Journal, Series B 37, 369–376.

Schewe, G., 1983. On the force fluctuations acting on a circular cylinder in cross-flow from subcritical up to transcritical Reynolds numbers. Journal of Fluid Mechanics 133, 265–285.

Sumner, D., Richard, M.D., 2003. Some vortex-shedding characteristics of the staggered configuration of circular cylinders. Journal of Fluids and Structures 17, 345–350.

Sumner, D., Price, S.J., Paidoussis, M.P., 2000. Flow-pattern identification for two staggered circular cylinders in cross-flow. Journal of Fluid Mechanics 411, 263–303.

Sun, T.F., Gu, Z.F., He, D.X., Zhang, L.L., 1992. Fluctuating pressure on two circular cylinders at high Reynolds number. Journal of Wind Engineering and Industrial Aerodynamics 41–44, 77–588.

Tang, Y.P., Rockwell, D., 1983. Instantaneous pressure fields at a corner associated with vortex impingement. Journal of Fluid Mechanics 126, 187–204.

Ting, D.S.K., Wang, D.J., Price, S.J., Paidoussis, M.P., 1998. An experimental study on the fluidelastic forces for two staggered circular cylinders in cross-flow. Journal of Fluids and Structures 12, 259–294.

Wardlaw, R.L., Cooper, K.R., 1973. A wind tunnel investigation of the steady aerodynamic forces on smooth and stranded twin bundled power conductors for the Aluminum Company of America. National Research Council of Canada, LTR-LA-117.

Williamson, C.H.K., 1996. Three dimensional wake transition. Journal of Fluid Mechanics 328, 345–407.

Ziada, S., Rockwell, D., 1982. Vortex–leading-edge interaction. Journal of Fluid Mechanics 118, 79–107.

Zdravkovich, M.M., 1977. Review of flow interference between two circular cylinders in various arrangements. ASME Journal of Fluids Engineering 199, 618–633.

Zdravkovich, M.M., 1980. Aerodynamics of two parallel circular cylinders of finite height at simulated high Reynolds numbers. Journal of Wind Engineering and Industrial Aerodynamics 6, 59–71.

Zdravkovich, M.M., 1984. Classification of flow-induced oscillations of two parallel circular cylinders in various arrangements. ASME Winter Annual Meeting, Symposium on Flow-Induced Vibrations, vol. 2, pp. 1–18.

Zdravkovich, M.M., 1987. The effects of interference between circular cylinders in cross flow. Journal of Fluids and Structures 1, 239–261.

Zdravkovich, M.M., 1997. Flow around circular cylinders. Volume 1. Fundamentals. Oxford Science Publications, New York.

Zdravkovich, M.M., Pridden, D.L., 1977. Interference between two circular cylinders; series of unexpected discontinuities. Journal of Industrial Aerodynamics 2, 255–270.